Collings, R., Rietbrock, A., Tilmann, F., Lange, D., Nippres, S., Natawidjaja, D. (2013): Seismic anisotropy in the Sumatra subduction zone. - *Journal of Geophysical Research*, *118*, 10, 5372-5390

DOI: 10.1002/jgrb.50157

JOURNAL OF GEOPHYSICAL RESEARCH: SOLID EARTH, VOL. 118, 5372–5390, doi:10.1002/jgrb.50157, 2013

Seismic anisotropy in the Sumatra subduction zone

R. Collings,[1] A. Rietbrock,[1] D. Lange,[2] F. Tilmann,[3,5] S. Nippress,[1] and D. Natawidjaja[4]

Received 3 July 2012; revised 1 March 2013; accepted 8 March 2013; published 8 October 2013.

[1] An important tool for understanding deformation occurring within a subduction zone is the measurement of seismic anisotropy through observations of shear wave splitting (SWS). In Sumatra, two temporary seismic networks were deployed between December 2007 and February 2009, covering the fore arc between the fore-arc islands to the back arc. We use *SKS* and local SWS measurements to determine the type, amount, and location of anisotropy. Local SWS measurements from the fore-arc islands exhibit trench-parallel fast directions which can be attributed to shape preferred orientation of cracks/fractures in the overriding sediments. In the Sumatran Fault region, the predominant fast direction is fault/trench parallel, while in the back-arc region it is trench perpendicular. The trench-perpendicular measurements exhibit a positive correlation between delay time and raypath length in the mantle wedge, while the fault-parallel measurements are similar to the fault-parallel fast directions observed for two crustal events at the Sumatran Fault. This suggests that there are two layers of anisotropy: one due to entrained flow within the mantle wedge and a second layer within the overriding crust due to the shear strain caused by the Sumatran Fault. *SKS* splitting results show a NNW-SSE fast direction with delay times of 0.8–3.0 s. The fast directions are approximately parallel to the absolute plate motion of the subducting Indo-Australian Plate. The small delay times exhibited by the local SWS (0.05–0.45 s), in combination with the large SKS delay times, suggest that the anisotropy generating the teleseismic SWS is dominated by entrained flow in the asthenosphere below the slab.

Citation: Collings, R., A. Rietbrock, D. Lange, F. Tilmann, S. Nippress, and D. Natawidjaja (2013), Seismic anisotropy in the Sumatra subduction zone, *J. Geophys. Res. Solid Earth*, *118*, 5372–5390, doi:10.1002/jgrb.50157.

1. Introduction

[2] Anisotropy is the directional dependence of seismic velocity within a material. When a shear wave propagates through an anisotropic medium, it is split into two independent waves with polarizations perpendicular to each other, which travel at different velocities. The component that is polarized parallel to the direction of fast seismic velocity travels faster than the orthogonal component, causing shear wave splitting (SWS) [*Silver and Chan*, 1988, 1991; *Vinnik et al*., 1989]. Two parameters are measured: the orientation of the fast shear wave and the delay time between the two arrivals. The time lag between the two arrivals provides information on the product of the strength of anisotropy and the thickness of the anisotropic layer.

[3] Since the early observations of SWS [*Ando et al*., 1983; *Fukao*, 1984], subduction zones have been among the most popular targets for SWS studies. An astonishing diversity in SWS patterns [e.g., *Greve et al*., 2008; *Hammond et al*., 2010; *Long and van der Hilst*, 2005] has been identified in different regions from both local *S* phases and teleseismic phases such as *SKS*, including both trench-parallel and trench-perpendicular fast polarization directions (with some oblique directions as well) and widely variable delay time values. In fact, it is common for SWS observations to vary within a single subduction zone. This variation in SWS observations reflects the complex structure of subduction zones with contributions to the SWS coming from various parts of the subducting system: the subslab mantle, the subducting slab, the mantle wedge and the overlying crust.

[4] It is widely accepted that seismic anisotropy generated in the upper mantle is dominated by lattice preferred orientation (LPO) in olivine. At these depths, olivine is volumetrically abundant and has significant single-crystal shear wave anisotropy of 18% [*Mainprice*, 2007]. LPO measured in naturally deformed peridotite rocks [*Christensen*, 1984; *Nicolas and Christensen*, 1987] and in samples deformed in the laboratory [*Zhang and Karato*, 1995] suggest that the fast axis of olivine (*a* axis) tends to align with the maximum shear direction or mantle flow direction [*Babuška and Cara*, 1991; *Mainprice et al*., 2000; *Mainprice*, 2007]. These experimental observations and the fact that SWS fast polarization directions are shown to align with relative plate

Additional supporting information may be found in the online version of this article.

[1]University of Liverpool, Liverpool, UK.
[2]University of Potsdam, Potsdam, Germany.
[3]GFZ German Research Centre for Geosciences, Potsdam, Germany.
[4]Lab Earth, Indonesian Institute of Sciences (LIPI), Bandung, Indonesia.
[5]Freie Universität Berlin, Berlin, Germany.

Corresponding author: A. Rietbrock, University of Liverpool, 4 Brownlow Street, Liverpool L69 3GP, UK. (A.Rietbrock@liverpool.ac.uk)

2169-9313/13/10.1002/jgrb.50157

motion [e.g., *Hall et al*., 2000; *Nippress et al*., 2007] allowed seismologists to gain direct information about dynamic processes such as mantle flow. However, over the last decade, a series of experiments [*Katayama et al*., 2004; *Jung et al*., 2006; *Katayama and Karato*, 2006] have shown that the orientation of the fast axis of olivine does not always align with the maximum shear direction but is dependent upon stress, temperature, and water content. So there are now in fact five different types of olivine LPO: the original A type plus B, C, D, and E types. In B-type anisotropy, which occurs at high differential stresses and hydrous conditions, the *a* axis aligns orthogonal to the shear direction not parallel as usual.

[5] Seismic anisotropy can also develop from shape preferred orientation (SPO). SPO occurs when orientated cracks, faults, fractures, melt filled inclusions, compositional layering, or lenses make an otherwise homogeneous medium anisotropic for wavelengths larger than the space interval [*Backus*, 1962]. It is widely accepted that seismic anisotropy in the upper crust is dominated by SPO [e.g., *Crampin*, 1994]. Crustal anisotropy develops predominantly in the upper 10–15 km of the crust due to cracks and microcracks aligned with the direction of maximum stress [*Crampin*, 1994]. However, in regions that contain large structural features, e.g., strike-slip faults, anisotropy is formed by fault-parallel aligned minerals and fractures that have developed from shearing along the plate boundary [*Kaneshima*, 1990; *Gledhill and Stuart*, 1996; *Savage*, 1999].

[6] A global data set of SWS observations [*Long and Silver*, 2008] using teleseismic *SKS* phases (delay times generally >1.0 s) with contributions from mantle wedge anisotropy removed is dominated by trench-parallel fast directions. However, there are several regions that show trench-perpendicular fast polarization directions including the Juan de Fuca slab beneath Cascadia, the Middle America subduction zone beneath Mexico, and in northern and south-central Chile. *Long and Silver* [2008] attribute the observed trench-parallel SWS observations to trench migration with a model where the slab is decoupled from the subslab mantle (due to shear heating of hot buoyant asthenosphere and subsequent entrainment of a thin asthenospheric layer decoupling the slab from the mantle), with a partial barrier to flow (at the top or bottom of the transition zone) which forces upper mantle material to move parallel to the trench. This trench-parallel subslab flow generates A-type olivine LPO that agrees with the *SKS* trench-parallel SWS measurements observed at most subduction zones around the world. The previously mentioned exceptions can be explained by entrainment of asthenospheric mantle by the subducting slab. Based on geodynamic modeling, *Hicks et al*. [2012] concluded that the observed SWS results in south-central Chile can be explained with a thick dipping layer of subslab entrained asthenosphere. *Long and Silver* [2008] also suggest that trench migration could cause trench-parallel flow within the mantle wedge, which would explain the trench-parallel splitting observation recorded from local shear waves in Tonga [*Smith et al*., 2001], Central America [*Hoernle et al*., 2008; *Abt et al*., 2009], Marianas [*Pozgay et al*., 2007], and Kamchatka [*Levin et al*., 2004]. An alternative explanation is put forward by *Jung and Karato* [2001] and *Jung et al*. [2009] who report experimental data suggesting that the subslab mantle and the supramantle are dominated by B-type olivine fabric. This would imply that the observed trench-parallel fast directions beneath slabs and within mantle wedges are due not to trench-parallel flow but to entrained flow and 2-D corner flow in the subslab region and mantle wedge, respectively.

[7] Alternative models have been proposed to explain these teleseismic SWS observations and suggest that the slab is anisotropic. Numerical models [*Faccenda et al*., 2008] invoke the hydration and serpentinization of trench-parallel faults that penetrate the lithospheric slab as a mechanism for generating trench-parallel teleseismic SWS. A last possibility is fossilized anisotropy in the downgoing subducting slab [e.g., *Hammond et al*., 2010]. As oceanic lithosphere is formed and moves over the asthenosphere, the fast axes of the anisotropic minerals (e.g., olivine) are aligned in the direction of plate motion (e.g., at the East Pacific Rise) [*Wolfe and Solomon*, 1998; *Harmon et al*., 2004]. These anisotropic characteristics can be frozen into the lithosphere and may remain present in the subducted slab. However, it is unclear what portion of the slab is capable of retaining this fossilized deformation: the whole slab or just the central core, which is subject to the least amount of deformation as the slab subducts.

[8] Recent studies [*Hammond et al*., 2010; *Tono et al*., 2009] have shown the importance of measuring SWS using both local and teleseismic arrivals in the same region to constrain the depth dependence of anisotropy. Using local earthquakes beneath Java-Sumatra, *Hammond et al*. [2010] report SWS observations that show trench-parallel fast directions, with 0.1–1.0 s (92% $\leq$0.6 s) delay times. SWS observations from *SKS* phases show larger delay times (0.8–2.0 s), with fast polarization directions beneath Sumatra parallel (Figure 1) to the absolute plate motion (APM) and trench-parallel beneath Java. *Hammond et al*. [2010] explain the SWS from local events with anisotropy confined to the upper 40 km of the overriding plate with horizontal, trench-parallel deformation and the larger delay times from *SKS* phases by significant fossilized anisotropy within the slab itself. The observed change in *SKS* fast polarization direction correlates well with a significant change in plate age from $>$100 Ma in Java to $<$100 Ma beneath Sumatra and might indicate a fundamental change in mantle flow.

[9] The substantial variation in the recorded splitting measurements at subduction zones and the range of mechanisms to explain the observations show that subduction zones are complicated environments. In this study, we use SWS observations on a dense temporal array from the Sumatran subduction zone to improve our understanding of the style and geometry of deformation within subduction zone setting.

2. Tectonic Setting

[10] The subduction of the Indo-Australian Plate beneath the Eurasian Plate has formed the Sunda Arc, which extends for 5600 km from the Andaman Islands in the northwest to the Banda Arc in the southeast (Figure 1). The island of Sumatra is located on the overriding plate of the Sunda Arc between the Sunda Strait, in the south, and the Andaman Islands, in the north (Figure 1).

[11] On the subducting Indo-Australian Plate lies the Wharton Fossil Ridge, a bathymetric feature that is offset

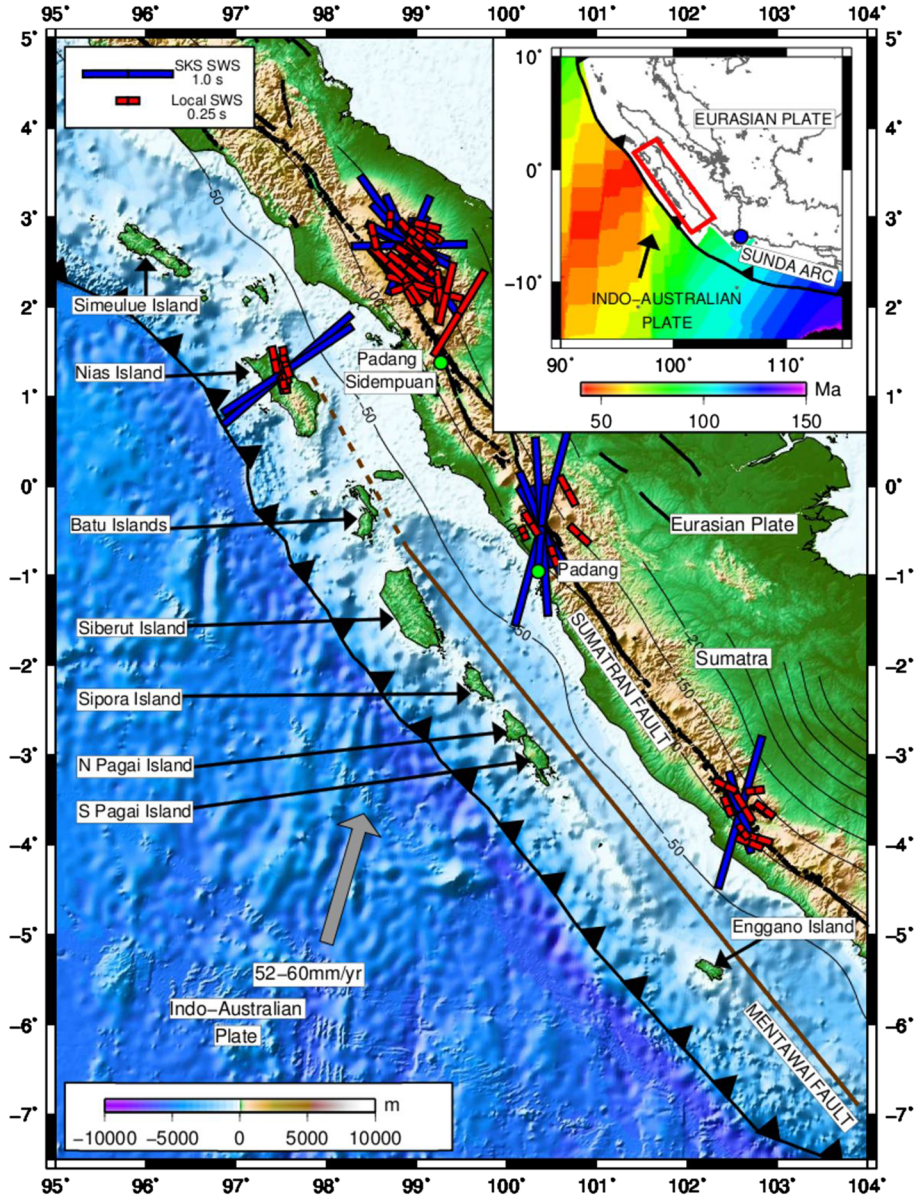

Figure 1. Map showing the West Sumatra subduction zone. The Indo-Australian Plate is moving toward the Eurasian Plate forming the Sunda Trench. The blue circles on the inset map of the Sunda Arc marks the position of the Sunda Strait, and the red box is the location of the study area. The age of the incoming Indo-Australian Plate along the Sunda Arc [*Müller et al*., 1997] is indicated on the inset map. On the main map, the location of the Mentawai Fault [*Diament et al*., 1992] (brown line) and the Sumatran Fault [*Sieh and Natawidjaja*, 2000] (black line) is shown. Black contours indicate the depth of the subducting slab (SLAB1.0) [*Hayes and Wald*, 2009]. The SWS observations of *Hammond et al*. [2010] are shown. Blue are *SKS* SWS measurements plotted at the station, while red are local SWS measurements plotted at the midpoint between event and station. The scale at the bottom left is bathymetry and topography.

by fossil transform faults, which are responsible for the variation in lithospheric age of the oceanic crust along the arc [*Deplus et al*., 1998]. The age of the crust increases from 49 Ma below North Sumatra (where the Wharton Fossil Ridge subducts) to 134 Ma below Java (Figure 1), which is reflected in the dip, temperature, and depth of the Wadati Benioff zone [*Shapiro et al*., 2008]. Adjacent to the Wharton Fossil Ridge, the subducting lithosphere is significantly more buoyant, warmer, and subducting at a shallower angle (30°) than regions further north or south, where the lithosphere is less buoyant, cooler, and dipping at 40°–50° [*Shapiro et al*., 2008]. In addition to the changing temperature, age, and dip of the subducting plate, along the Sunda Arc there is also a variation in the obliquity of the subduction (Figure 1). At the Sunda Strait, the subduction angle changes from normal subduction beneath Java to oblique subduction underneath Sumatra (~40° at 2° N), with a convergence rate that decreases from 60 mm/year at 6°S to 52 mm/year at 2°N [*Prawirodirdjo et al*., 2000] using the ITRF96 reference frame. A result of the oblique subduction

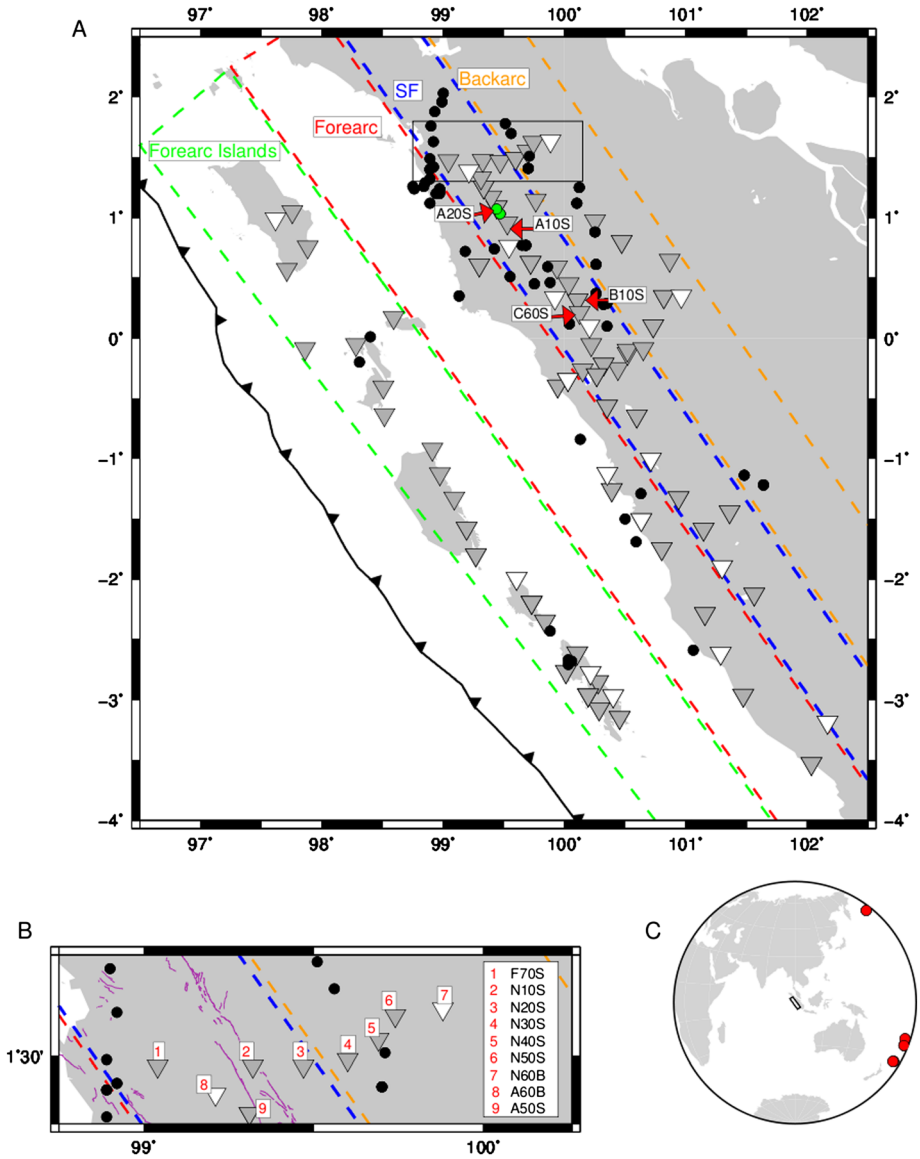

Figure 2. (a) Map showing station locations. Dark gray triangles indicate short period instruments, and white triangles show broadband instruments. The circles show the local events used in this study. Black circles show events at the slab interface or within the slab, and green circles show shallow events in the overriding crust. The study region is divided into four areas. The green dashed box is the fore-arc island region, the red dashed box is the fore-arc region, the blue dashed box is the Sumatran Fault region, and the orange dashed box is the back-arc region. The black box indicates the location of the area shown in Figure 2b. (b) A zoomed-in map of the stations in northern Sumatra. (c) Map showing the location of the teleseismic events. The red circles are the locations of the teleseismic events, and the black box is the study region.

is strain partitioning of the convergence into strike-slip motion and thrust motion. Strike-slip motion along the Sumatran margin is primarily accommodated by the Sumatran Fault, a large, highly segmented, strike-slip fault that extends for 1900 km from the Sunda Strait to the Andaman sea across Sumatra, parallel and in close proximity to the volcanic arc [e.g., *Sieh and Natawidjaja*, 2000].

3. Data and Method

[12] Between December 2007 and February 2009, two seismic networks were installed in southern and central Sumatra (Figure 2), as well as the adjacent Mentawai, Nias, Batu, and Siberut Islands, at two different time periods which overlapped by 6 months. The southern network, the Mentawai network, was installed in western Sumatra between 1°S and 4°S [*Collings et al.*, 2012] and consisted of 18 CMG-6TD and 9 Trillium 120P instruments sampling at 50 and 100 Hz, respectively. The sensitivity of the CMG-6TD is up to 20 s and that of the Trillium 120P up to 120 s. The network was decommissioned in October 2008. The second deployment was in central/northern Sumatra on the mainland, between Padang Sidempuan and Padang, as well as on Nias Island, Siberut Island, and the Batu Islands

[*Lange et al*., 2010]. The dense northern network was operational between April 2008 and February 2009, and comprised 52 three-component stations with sampling rates of 50 and 100 Hz, including 7 broadband stations (CMG-3T with sensitivity up to at least 240 s).

[13] Prior to conducting the SWS analysis, the seismic traces were band-pass filtered to improve the signal-to-noise ratio and increase the stability of the SWS measurements. *SKS* waveforms, originating from earthquakes at epicentral distances between 85° and 140°, were filtered between 0.05 and 0.3 Hz, while local *S* waves, arriving at incidence angles of 35° or less (i.e., within the shear wave window [*Evans*, 1984]), were filtered between 0.1 and 3 Hz. The filter bands are thus within the sensitivity range of the instruments. The overlap in the filter bands between the *SKS* and local *S* waves minimizes the frequency-dependent effects between the two data sets [*Hammond et al*., 2010] (see Figures S1 and S2). Locations for the local events were determined from a 3-D velocity model in the Mentawai region [*Collings et al*., 2012] and a minimum 1-D velocity model in the central/North Sumatra region [*Lange et al*., 2010]. Eighty-five percent of the analyzed local events were recorded by the central/northern network, with the majority (90%) located between 70 and 200 km depth, within a broad 200 km wide zone that corresponds to an area of rough seafloor topography. In particular, the N-S linear streak of seismicity at 99°E 1.5°N coincides with the projected prolongation of a fracture zone [*Lange et al*., 2010]. Jack-knife tests were performed to estimate the accuracy of the hypocenters. The average standard deviation was 1.1 km in the horizontal direction and less than 2.0 km in depth [*Lange et al*., 2010].

[14] For local SWS analysis, we used the program SHEBA [*Teanby et al*., 2004], which is based on the eigenvalue methodology of *Silver and Chan* [1991]. For the teleseismic phases, we used both SHEBA and SplitLab [*Wüstefeld et al*., 2008]. The advantage of using SplitLab is that SWS estimates are calculated using three independent methods: eigenvalue [*Silver and Chan*, 1991], rotation and correlation [*Bowman and Ando*, 1987], and minimum transverse energy [*Silver and Chan*, 1991]. Only *SKS* SWS measurements that were stable in both SplitLab and SHEBA were included in this study. In both SHEBA and SplitLab, automated SWS analysis is used. This enables the fast direction (Φ) and the splitting delay time (δt) to be calculated for a range of time windows within an initially manually selected range, with the optimum Φ and δt values found using cluster analysis [*Teanby et al*., 2004]. The resulting Φ and δt are not necessarily the results that produce the smallest error bars but are the results that are stable over various sizes of analysis windows.

4. Results

[15] To assess the stability and quality of a SWS observation, a number of quality control tests were performed. If a shear wave has passed through an anisotropic medium, the splitting can be identified visually by elliptical particle motion; for *SKS* waves, significant energy on the transverse component is another indicator of horizontal anisotropy. After correction, in which both components have been rotated by Φ and one lagged by δt, the particle motion should become linear, the fast and slow waves should align, and, for *SKS* measurements, the energy should be minimized on the corrected transverse component. If an observed SWS measurement did not exhibit this pattern, it was rejected. Errors on the splitting parameters must also be as low as possible. The errors are estimated using the inverse *F* test, which determines a confidence region for the SWS parameters [*Silver and Chan*, 1991]. Any SWS observations with 1σ errors greater than 0.4 s in δt and 30° in Φ were discarded.

[16] For *SKS* phases, the polarization of the shear wave after the anisotropy correction was compared to the backazimuth. *SKS* phases should have been radially polarized during the *P* to *S* conversion at the core mantle boundary, so their source polarization and backazimuth should be similar; results in which they differed by more than 30° were rejected as this can indicate instability in the SWS measurement [e.g., *Hammond et al*., 2010].

[17] In addition to these methods following *Wüstefeld and Bokelmann* [2007], we consider the difference in the fast directions and ratio of the delay times of the SWS measurements obtained using the rotation correlation and minimum transverse energy method. Based on synthetic tests, splitting measurements are defined as good if the delay time ratio between the two methods is between 0.7 and 1.2 and the fast axis misfit is less than 15°.

4.1. Teleseismic Splitting Results

[18] A total of 20 *SKS* SWS observations from 4 events at 16 stations produced stable splitting results using both SHEBA and SplitLab (Figure 3, black SWS results, and Table S1; waveform example in Figure S3). An additional five observations produced stable results in all three SWS techniques; however, the delay time ratios were not between 0.7 and 1.2 s and the misfits were >15° (Figure 3, light blue measurements, and Table S2). The good splitting measurements exhibit a consistent NNW to SSE fast direction, with an average fast direction of −10°. The average fast direction was calculated using a modified method of averaging directional data [*Audoine et al*., 2004], which was first described by *Krumbein* [1939] and applied to SWS fast directions by *Kubo and Hiramatsu* [1998]. The bidirectional nature of fast directions means that directional statistics, instead of simple Gaussian statistics, must be used to calculate the mean. The delay times of the 20 good results are spread between 0.8 and 3.0 s with 60% of the measurements lying between 1.6 and 2.4 s. The raypaths of the rays were calculated using the 2-D velocity model of *Collings et al*. [2012] merged with PREM for depths greater than 200 km. The 2-D tomographic model of *Collings et al*. [2012] was extrapolated to the NW beyond the area the model was developed for, and an additional inversion was run with events from both networks to obtain an approximate 2-D model for the fore arc. The raypaths show that the rays travel a substantial distance beneath the slab interface.

4.2. Local Splitting Results

[19] A total of 78 good local SWS measurements were obtained from 55 events at focal depths between 10 and 200 km. A good event was defined based on the criteria of *Teanby et al*. [2004] described above (Figure S4). The fast directions (Figure 4a) are scattered, but they indicate two

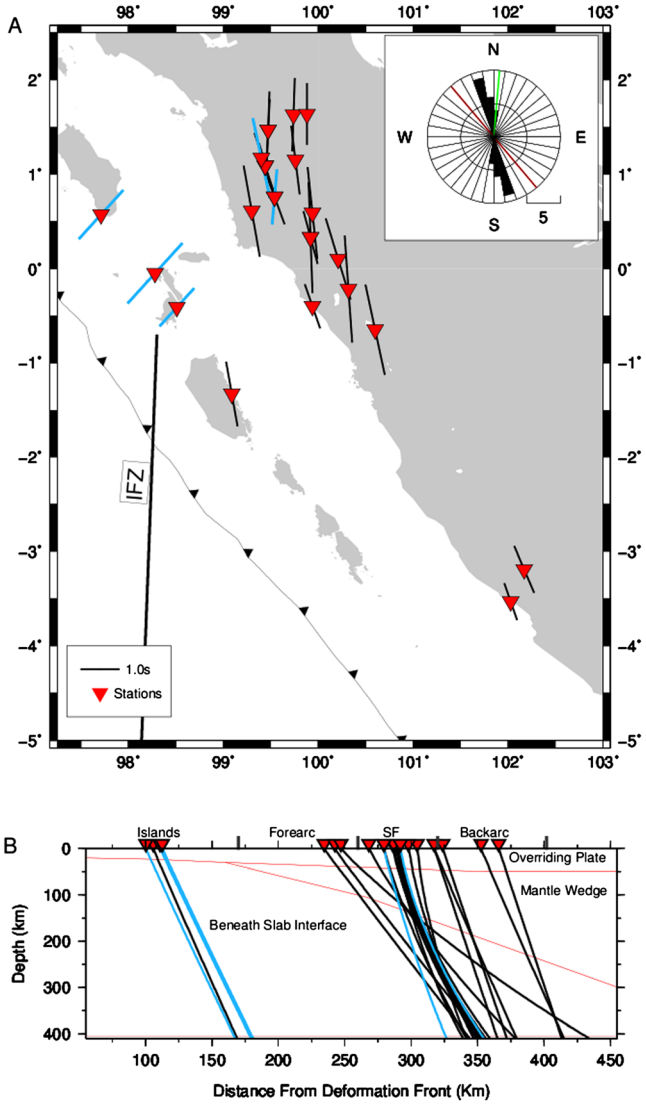

Figure 3. (a) *SKS* SWS results using the minimum transverse energy method. Back measurements indicate good SWS results, while blue indicated stable SWS results but they were not classed as good. The measurements are plotted at the station. The position of the investigator fracture zone (IFZ) is indicated. The rose diagram shows the orientation of the SWS fast directions. The orientation of the trench is indicated by the red line, and the convergence direction is indicated by the green line. (b) Profile showing the raypaths of teleseismic events together with the main structures of the margin from *Collings et al*. [2012].

predominant directions: NW-SE (trench parallel) and ENE-WSW (trench perpendicular). The delay times are spread between 0.05 and 0.45 s. The results show a weak positive correlation between source depth and delay time for events deeper than 75 km (Figures 5c and 5d). This suggests that these rays sample a uniformly anisotropic structure in which the longer the wave spends in the structure, the greater the magnitude of the splitting.

[20] Due to the observed spread in fast directions (Figure 4a), the local splitting results were analyzed in four regions (fore-arc islands, fore arc, Sumatran Fault, and back arc; Figure 2a). The distance each ray spends in the mantle wedge and overlying crust was calculated using the 2-D tomographic model of *Collings et al*. [2012]. *P* velocities <7 km/s are indicative of crustal material, whereas typical mantle velocities are more than 8 km/s. Therefore, we used the 7.5 km/s contour to estimate the thickness of the crust. The crustal thickness appears to increase from 25 km within the fore-arc region to 50 km within the back-arc region [*Collings et al*., 2012]. Similarly, the thickness of the mantle wedge was estimated using the 7.5 km/s *P* velocity contour and the seismicity distribution of the earthquakes that are occurring along the plate interface and within the subducting plate. These distances were then plotted against observed delay times to identify trends (Figure 5).

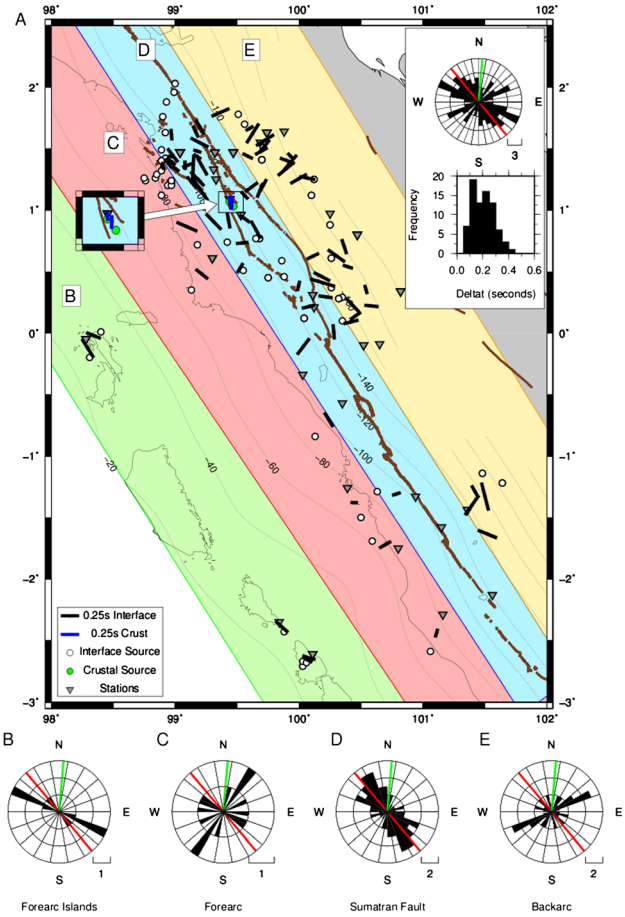

Figure 4. (a) Local SWS results using the eigenvalue method. All measurements are plotted at the midpoint between the event location (white circles) and station (grey triangles). Brown lines represent the faults within the region. The fore-arc island region (green), fore-arc region (red), Sumatra Fault region (blue), and back-arc region (orange) are colored. Inlay is showing a rose diagram with the SWS fast directions (in all rose diagrams, the orientation of the trench is indicated by the red line and the convergence direction is indicated by the green line) and a histogram of delay times. Rose diagrams of SWS fast directions are shown for events located in (b) the fore-arc island region, (c) the fore-arc region, (d) the Sumatran Fault region, and (e) the back-arc region.

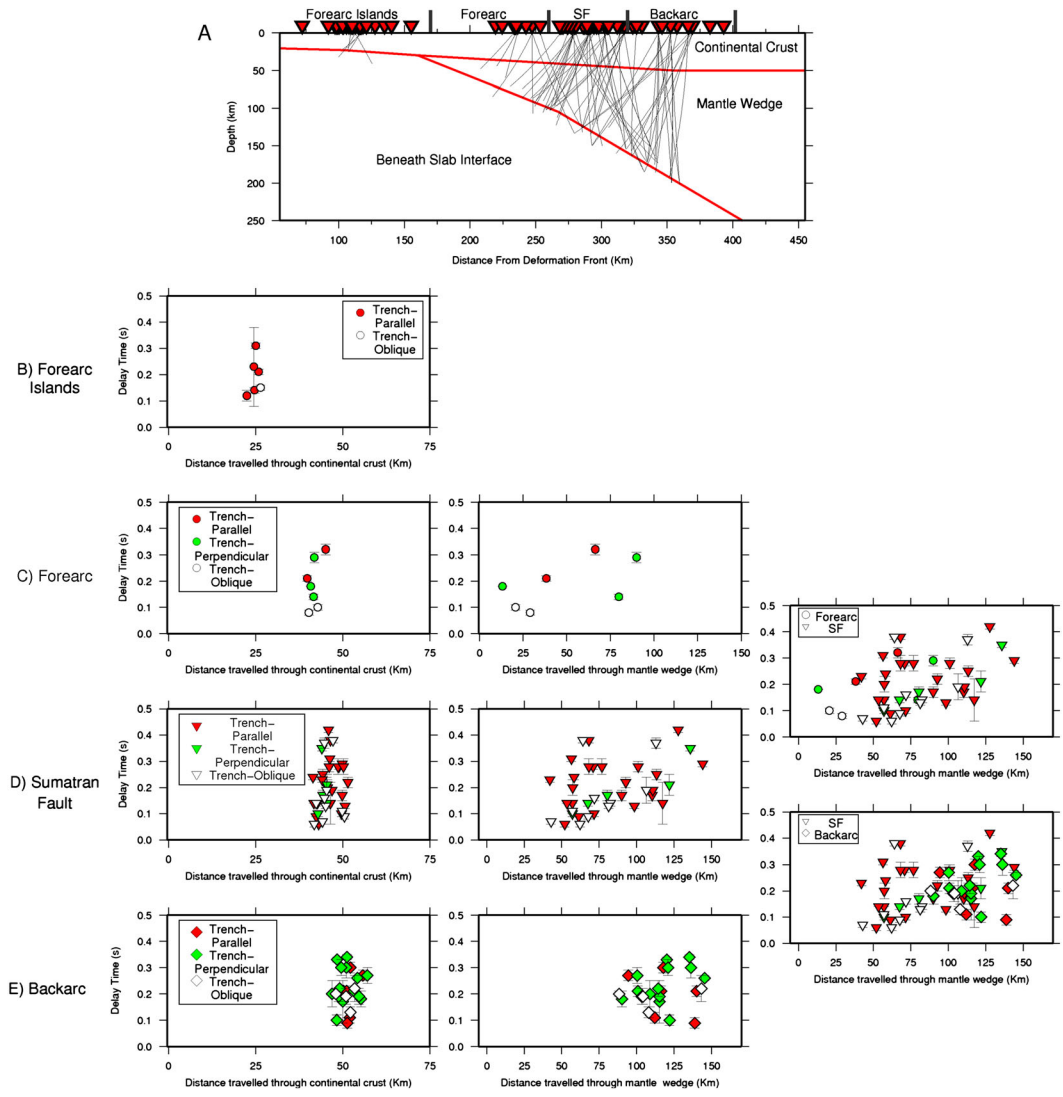

Figure 5. (a) Raypaths of local events traced through the local velocity model [from *Collings et al.*, 2012]. (b) Distance each raypath has spent within the crust versus delay time for events in the fore-arc island region. In all plots, red circles are fault/trench-parallel measurements, green circles are trench-perpendicular measurements, and white circles are trench oblique measurements. (c) Distance each raypath has spent within the crust (left) and mantle wedge (center) versus delay time for events in the fore-arc region. Right-hand graph is distance each raypath has spent within the mantle wedge versus delay time for events in the fore-arc and Sumatra Fault region. (d) Distance each raypath has spent within the crust (left) and mantle wedge (center) versus delay time for events in the Sumatran Fault region. Right-hand graph is distance each raypath has spent within the mantle wedge versus delay time for events in the Sumatran Fault and back-arc region. (e) Distance each raypath has spent within the crust (left) and mantle wedge (center) versus delay time for events in the back-arc region.

4.2.1. Fore-Arc Islands

[21] The six splitting measurements obtained from stations on the fore-arc islands exhibit a coherent approximate trench-parallel fast direction (Figure 4b and Table S3), with an average direction of −59° (see section 4.1 for averaging technique) and a circular deviation of 0.03. The circular deviation is a measure of deviation from the average. If all the measurements are aligned, the circular deviation is 0, and if they are poorly aligned, it is 1. δt is spread between 0.10 and 0.31 s. The rays travel for 20–25 km through accreted low-velocity sediments and do not travel through the mantle wedge (Figures 5a and 5b).

4.2.2. Fore Arc

[22] Only seven measurements were obtained in the fore-arc region with two results showing trench-parallel fast directions, three results exhibiting approximately trench-perpendicular fast directions, and two indicating trench-oblique fast directions (−88° and 16°) (Figures 4c and 5c and Table S4). The delay times vary between 0.08 and 0.32 s. All rays travel ~30 km in the continental crust (Figure 5a) and do not show any correlation with δt (Figure 5c). However, in the mantle wedge, there appears to be a weak positive correlation between distance traveled and δt.

4.2.3. Sumatran Fault

[23] Although fast directions both perpendicular and parallel to the trench/Sumatran Fault are observed in the Sumatran Fault region (Table S5), the predominant fast direction is trench/fault parallel (Figure 4d), which results in an average fast direction of −14°, with a circular deviation of 0.24. The delay times are between 0.06 and 0.42 s. Splitting measurements from two events at the Sumatran Fault, located at ~13 km (therefore only traveling within the crust), exhibit fast directions that are approximately N-S with delay times of 0.10 to 0.17 s (Figure 4a, blue measurements). Although this is oblique to the general NW-SE trend of the fault and trench, in this region the Sumatran Fault trends in a more N-S direction, which is approximately parallel to the fast directions of the two crustal events. Only two SWS measurements were obtained from crustal events as the events have to occur almost directly beneath the station to ensure the angle of incidence was less than 35°. Also, the data from these events were often noisy, producing unstable splitting result. Events at the slab interface and within the slab travel between 35 and 50 km in the crust (Figure 5a) and show no correlation of fast direction or delay time with distance traveled (Figure 5d). A positive correlation can be seen between distance traveled in the mantle wedge and delay time (Figure 5d). The relationship is particularly evident for the trench-perpendicular measurements.

4.2.4. Back Arc

[24] In the back arc, both trench-parallel and trench-perpendicular fast directions are present (Table S6), but the predominant direction is trench perpendicular (Figures 4a and 4e). The delay times vary between 0.09 and 0.34 s. The previous positive correlation observed in the fore-arc and Sumatran Fault region between distance traveled in the mantle wedge and δt is not as evident in the back-arc region (Figure 5e). However, when separating the trench-parallel and trench-perpendicular results, this relationship is more noticeable again for the trench-perpendicular measurements (Figure 5e, green measurements). The trench-parallel results remain scattered (Figure 5e, red measurements).

5. Discussion of Local *S* Splitting and Possible Mechanisms

[25] The study of *Hammond et al*. [2010] concluded that the mantle wedge was nearly isotropic (0.3% anisotropy) as no relationship between event depth and delay time was evident. Instead, the observed SWS was attributed to anisotropy in the overriding plate, caused by a 40 km layer of vertically aligned cracks [*Hammond et al*., 2010]. The amount of data and station coverage presented here is greater, and raypaths were calculated using local earthquake tomography [*Collings et al*., 2012], which allows a more in-depth analysis. A first-order feature of the local SWS observations in this study is the rotation in fast direction from a predominant trench-parallel direction close to the Sumatran Fault to a more trench-perpendicular direction further into the back arc. A transition from trench-parallel to trench-perpendicular splitting is also observed at several other subduction regions around the world such as northeast Japan [*Huang et al*., 2011] and Tonga [*Smith et al*., 2001]. The SWS observations show a positive relationship between length of raypath spent within the mantle wedge and delay time, suggesting that anisotropy is present within the mantle wedge. In this study, two splitting measurements from earthquakes along the Sumatran Fault, at ~13 km depth, exhibit fast directions that are approximately parallel to the surface trace of the Sumatran Fault in that region, with delay times of 0.10–0.17 s, suggesting a crustal component of anisotropy within this region.

5.1. Fore-Arc Islands

[26] Previously, trench-parallel fast directions close to the subduction trench have been attributed to either B-type olivine fabric [*Jung and Karato*, 2001] or the effect of slab rollback on mantle flow [*Smith et al*., 2001]. It is clear from the raypaths of the events beneath the fore-arc islands (Figure 5a) that these rays do not travel through the mantle wedge, and therefore, the anisotropy must be located within either the overriding sediment or the subducting slab. The fore-arc islands are composed of low-velocity sediments that were part of a former accretionary prism before being uplifted to form the fore-arc islands [*Kopp et al*., 2001; *Collings et al*., 2012]. Anisotropy in the low-velocity sediments beneath the fore-arc islands may therefore result from the alignment of cracks and minerals which could have occurred during uplift, when the former accretionary prism was subjected to a high amount of deformation. The hypocenter locations and local earthquake tomography in *Collings et al*. [2012] also show that, beneath the fore-arc islands, the subducting slab is hydrated and faulted which could also contribute to the observed local SWS. The trench-parallel fast directions at the fore-arc islands in Sumatra are similar to northeast Japan [*Huang et al*., 2011] where trench-parallel splitting measurements in the fore arc have recently been attributed to aligned cracks within the overriding crust and either fossilized anisotropy (LPO orientation of crystals) or the alignment of cracks within the subducting slab.

5.2. Fore-Arc, Sumatran Fault, and Back-Arc Regions

5.2.1. Trench-Perpendicular Measurements

[27] In the fore-arc, back-arc, and Sumatran Fault region, a positive correlation is observed between raypath length in the mantle and delay time (Figures 5c–5e). This relationship is particularly evident for the trench-perpendicular splitting measurements in the Sumatran Fault and back-arc regions. The average delay time is 0.21 s which is small compared to Tonga and Ryukyu where a $\delta t > 1.0$ s has been observed for events at 75–100 km depth [*Smith et al*., 2001; *Long and van der Hilst*, 2006]. In Sumatra, only a small amount of splitting is suggested to occur within the mantle wedge itself as the maximum delay time for a slab earthquake, which exhibits approximately trench-perpendicular fast directions, is 0.35 s. *Long and Silver* [2008] hypothesize that anisotropy in the mantle wedge beneath the fore arc and arc is controlled by competing influences of two flow fields, 2-D corner flow and 3-D flow, whose relative importance is governed by the magnitude of the trench velocity normalized by the convergence velocity ($V_{norm} = |V_t|/V_c$). When $V_{norm} \leq \sim 0.2$, downdip motion dominates, resulting in 2-D corner flow, and when $V_{norm} \geq 0.6$, trench migration/advance dominates, resulting in a 3-D flow field; between these two regimes, small delay times are recorded as neither 2-D nor

3-D flow dominates. At Sumatra, V_{norm} is calculated to be ~0.3 [*Long and Silver*, 2008] which suggests that the two flows are competing, resulting in an incoherent flow field which can change rapidly over short length scales and, as a consequence, causes only a small amount of splitting. This agrees with the SWS observations for the fore-arc region where various splitting directions are observed. Despite a positive correlation between delay time and length of raypath in the mantle wedge, implying that anisotropy is occurring within the mantle wedge, there is no predominant fast direction. Therefore, neither 2-D corner nor 3-D flow appears to dominate and the delay times are small. In the back-arc region, the predominant fast direction is trench perpendicular, and in both the Sumatra Fault and back-arc regions, the trench-perpendicular SWS measurements exhibit a positive correlation between delay time and mantle distance. This relationship is not as evident for the trench/fault-parallel and trench-oblique measurements, but some correlation is still present. This suggests that the source of splitting for the trench-perpendicular measurements is in the mantle wedge due to corner flow, though the delay times imply that the anisotropy created is not strong. This is similar to SWS observations in northeast Japan [*Huang et al*., 2011] where only 0.16 s of SWS is thought to occur in the mantle wedge due to the center of the mantle wedge being weakly anisotropic or isotropic. The predominant trench-perpendicular direction observed within the back-arc region suggests that in this region, the influence of trench migration on mantle flow is reduced; 2-D corner flow should therefore dominate and result in trench-perpendicular fast directions [*Long and Silver*, 2008]. We therefore attribute the observed trench-perpendicular fast directions in the back-arc region and Sumatra Fault regions to 2-D corner flow in the mantle wedge, which is induced by the viscous coupling between the subducting slab and the overlying mantle [*Ribe*, 1989]. As the slab subducts, mantle wedge material is dragged down by viscous flow along the slab surface. The dragged down material is then passively replaced by hot and low-viscosity mantle materials from deeper within the mantle wedge, resulting in an upward return flow. This generates seismic anisotropy which is suggested to be dominated by the LPO of olivine, as the fast axis of olivine (*a* axis) aligns with the mantle flow direction. Numerical modeling [*Honda and Yoshida*, 2005; *Nakajima et al*., 2006] has shown that the return flow is parallel to the maximum dip of the slab and, therefore, at nonoblique subduction zones, parallel to the convergence direction. In Sumatra, however, where oblique subduction is occurring, the expected return flow is oblique to the convergence direction but perpendicular to the strike of the trench.

5.2.2. Trench/Sumatran Fault-Parallel SWS Observations

[28] Within the Sumatran Fault region and isolated areas of the back arc, observed SWS fast directions are approximately parallel to the trench or to the Sumatran Fault. Trench-parallel fast directions previously have been attributed to trench-parallel flow within the mantle wedge resulting from trench migration [*Smith et al*., 2001; *Long and Silver*, 2008]. As discussed above, the normalized trench migration/trench convergence value of 0.3 indicates that no coherent flow dominates in the mantle wedge, suggesting that isolated regions of 3-D flow could occur and create trench-parallel flow. Trench-parallel fast directions could also originate from B-type olivine fabric; it can develop within the mantle wedge when the water content and stress conditions are high [*Jung and Karato*, 2001]. Despite these possible mechanisms, we disregard anisotropy in the mantle wedge as the cause of the trench-parallel fast directions for a number of reasons. First, we do not observe a clear correlation between delay time and distance traveled within the mantle wedge for trench-parallel directions. Second, in the vicinity of the Sumatran Fault and within the back-arc region, we would expect the influence of trench migration to diminish [*Long and Silver*, 2008]. Finally, experimental results [*Jung and Karato*, 2001] and geodynamical modeling [*Lassak et al*., 2006] suggest that B-type olivine only develops in limited regions, specifically the fore-arc corner, and therefore should not be found in the Sumatran Fault and back-arc regions. For the Mentawai region, the local earthquake tomography [*Collings et al*., 2012] does not indicate the elevated *Vp/Vs* ratio, which would be expected for the high water content that could facilitate the development of B-type olivine LPO.

[29] Another possible explanation for the trench-parallel fast directions is that they originate from anisotropy within the crust. Crustal anisotropy [*Crampin*, 1994] has previously been attributed to cracks that are aligned with the maximum compressive stress direction and can result in 1.5% anisotropy in intact rocks and up to 10% anisotropy in very fractured rocks. In Sumatra, the maximum horizontal stress direction in the overriding Eurasian Plate is NE to SW [*Mount and Suppe*, 1992; *Tingay et al*., 2010], suggesting that it is not responsible for the observed trench/fault-parallel fast directions. In active fault zones regions, where cracks that have developed parallel to the maximum stress contain fluids at high pore pressures, a 90° flip in the fast polarization direction is observed [*Zatsepin and Crampin*, 1997; *Crampin et al*., 2002], which in Sumatra would result in fault-parallel fast directions. Despite this, we reject this mechanism as the cause of the trench-parallel observation, as the local earthquake tomography [*Collings et al*., 2012] and the minimum 1-D model of the upper crust along the Sumatran Fault [*Weller et al*., 2012] displays no evidence of significantly elevated *Vp/Vs* ratio in the continental crust, suggesting that no substantial fluids are present in the continental crust.

[30] Anisotropy in regions which contain large structural features, e.g., strike slip faults, has also been suggested to develop from preferential mineral alignment and orientated cracks and fractures [*Kaneshima*, 1990; *Gledhill and Stuart*, 1996; *Savage*, 1999]. This is true at the San Andreas Fault and Marlborough region of New Zealand, where many stations show fast directions consistently parallel to the strike of the faults, not the maximum compressive stress, and the anisotropy is attributed to mineral or fracture alignment caused by shearing along the plate boundary [*Zhang and Schwartz*, 1994; *Balfour et al*., 2005; *Gledhill and Stuart*, 1996; *Savage et al*., 2004]. At the San Andreas Fault, in order to explain all of the SWS observations, the anisotropy created by vertically orientated fault-parallel cracks/fractures and mineral alignment in North California has to be confined to a narrow area around the fault, while in Southern California the anisotropic layer either is thinner or does not exist [*Savage and Silver*, 1993; *Özalaybey and Savage*, 1995]. The situation at the San Andreas Fault is different to New Zealand where rays recorded at most stations in South North Island and in North South Island exhibit fast directions that are nearly parallel to the strike of the major strike slip faults (Alpine

Table 1. Fresnel Zone Radius and Overlap at Different Depths

Depth (km)	Fresnel Zone Radius (km)	Overlap (km)
50	8	no
75	10	yes
100	12	yes
150	14	yes

Fault, Marlborough fault system, North Island dextral fault belt), suggesting that the strain is distributed over a large area and that the crust, lithospheric upper mantle, and areas of the asthenospheric upper mantle are strongly coupled [*Klosko et al*., 1999; *Audoine et al*., 2000; *Savage et al*., 2004].

[31] In Sumatra, SWS measurements from two events originating on the Sumatran Fault, at a depth of ~13 km, exhibit fast directions approximately parallel to the surface trace of the Sumatran Fault in that region and delay times of 0.10–0.17 s, similar to delay times observed at the San Andreas Fault and the Marlborough region, New Zealand [*Zhang and Schwartz*, 1994; *Liu et al*., 2008; *Balfour et al*., 2005]. This implies that a layer of anisotropy is located within the upper crust due to the shear strain exerted by the Sumatran Fault. Slab earthquakes recorded at stations within the back-arc and Sumatran Fault region also exhibit trench/fault-parallel fast direction with larger delay times of up to 0.42 s, suggesting that deformation from simple shear extends deeper into the continental lithosphere and consequently could be masking any anisotropic signature from the 2-D corner flow occurring below in the asthenosphere. A thick layer of anisotropy within the overriding plate agrees with the results of *Hammond et al*. [2010] who attribute anisotropy to a 40 km layer of vertically aligned cracks. As the local SWS results do not exhibit a uniform fault-parallel direction throughout Sumatra, the shear strain is probably confined to a narrow region (~100 km) around the Sumatran Fault, which is similar to the SWS observations around the San Andreas Fault [*Savage and Silver*, 1993; *Özalaybey and Savage*, 1995]. This can be seen clearly in the northern area of our study region, at stations F70S, N10S, N20S, N40S, and N50S (Figure 2b). The two stations closest to the fault, N10S and N20S, as well as station F70S to the east where smaller strike-slip faults occur (Figure 2b), show approximate fault-parallel directions. Beyond this area, in the back arc, at stations N40S and N50S, the fast direction rotates to a predominant trench-perpendicular direction. In this region, a positive correlation is apparent between raypath length in the mantle and delay time (Figure 5e, trench-perpendicular measurements), suggesting that anisotropy is located within the mantle wedge from 2-D corner flow. We cannot rule out a small component of crustal anisotropy from microcrack alignment with the maximum stress direction (<0.1 s), but it is unlikely to be the main cause of anisotropy.

[32] The change in fast direction from fault parallel to trench perpendicular at stations N20S and N40S allows us to put some constraints on the location of anisotropy in this region [*Alsina and Snieder*, 1995]. To investigate whether two stations sample the same region, we calculate the Fresnel zone radius [*Sheriff and Geldart*, 1995].

$$\text{Fresnel zone radius} = \sqrt{\frac{V_s Z}{2f}}$$

where V_s is the shear velocity (average ~4 km/s) determined from the local earthquake tomography [*Collings et al*., 2012], Z is the depth, and f is the dominant frequency 1.5 Hz. This equation is only valid if $Z \gg V_s/f$, and as $V_s/f = 2.5$ km, we will only calculate the Fresnel zone radius for depths greater than 50 km.

[33] Stations N20S and N40S are ~26 km apart. The Fresnel zone radius calculation (Table 1) and the raypaths of two rays originating from the same event at 172 km depth suggest that the Fresnel zones will overlap at depths greater than 75 km. We can therefore conclude that rays arriving at station N40S and N20S, originating from the same hypocenter location, will sample the same region of the mantle wedge below ~75 km depth, but above this depth, they sample different regions of the mantle wedge and crust. Therefore the observed change in SWS can be attributed to lateral variations in anisotropy in the continental lithosphere and the upper part of the mantle asthenosphere (i.e., shallower than 75 km depth).

[34] Attributing the observed fast directions at stations above or close to the Sumatran Fault to aligned fractures and minerals caused by the NW-SE trend of the Sumatran Fault would predict a coherent fault-parallel fast directions at all stations on or close to the fault. Generally, nearby stations do show similar fault-parallel directions (e.g., at stations N20S, A20S, and F70S; Figure 2a); however, there are exceptions. At stations A50S, A10S, C60S, and B10S, which are situated above the Sumatran Fault, approximately trench/fault-perpendicular and trench/fault-oblique fast directions are observed. A possible explanation for these exceptions is that the Sumatran Fault is composed of numerous segments separated by dilational and contractional step overs, with abrupt changes in its trend [*Sieh and Natawidjaja*, 2000]. In addition to this, *Weller et al*. [2012] have found a complex set of faults bisecting the Sumatran Fault, which may also complicate the observed splitting. This suggests that the anisotropy induced by the structural fabric will not be consistently NW-SE throughout the lithosphere.

5.2.3. Two Layers of Anisotropy

[35] From the discussion above, it appears that two layers of anisotropy are present above the slab: an upper layer in the continental lithosphere due to the structural fabric induced by Sumatran Fault and a lower layer in the asthenospheric mantle wedge due to 2-D corner flow. When a wave traverses through two layers of anisotropy, the signal is split twice which can be identified by a $\pi/2$ periodicity in plots of δt and Φ versus source polarization [*Yardley and Crampin*, 1991; *Silver and Savage*, 1994]. It has been pointed out that at high frequencies (~25 Hz) and if one only looks at the signal onset, information about the lower layer is lost [*Yardley and Crampin*, 1991]. To ensure that information from the lower layer was not lost, the local S waves were band-pass filtered with corner frequencies of 0.1 and 3 Hz (10 and 0.33 s); therefore, the observed delay times (average 0.2 s) were smaller than the typical period. Here local S waves are being considered, whose source polarization is unknown prior to SWS analysis. Consequently, the best-fitting splitting parameters (Φ and δt) were determined using the eigenvalue methodology of *Silver and Chan* [1991]. The source polarization was then determined from the particle motion after anisotropy correction and linearization of the waveform. Therefore, the accuracy of the source

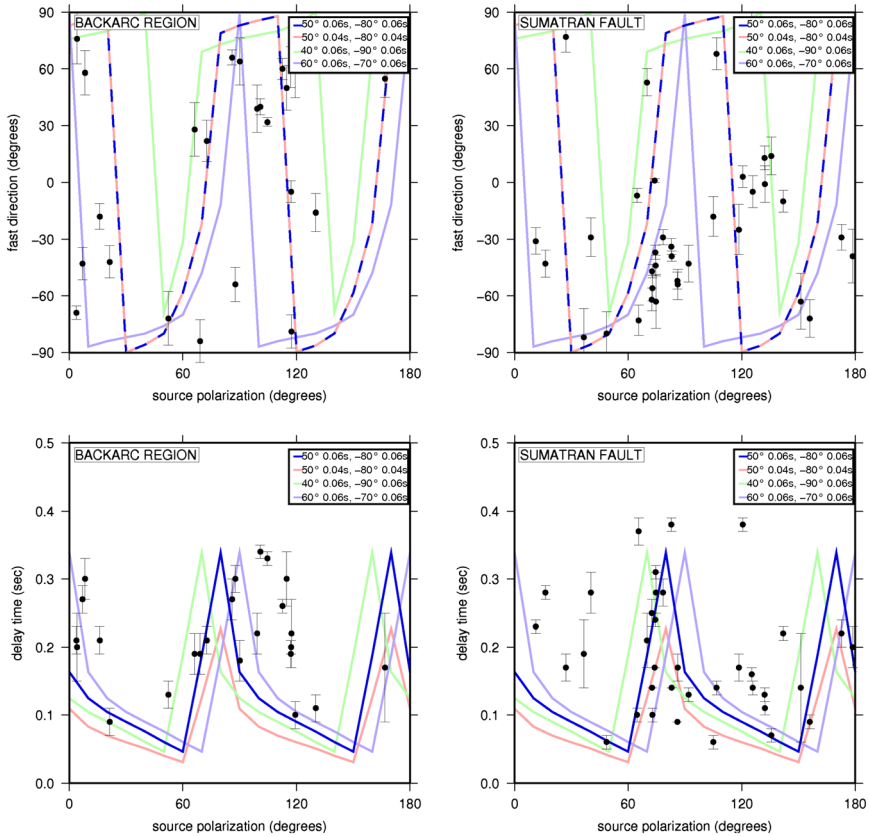

Figure 6. Comparisons of source polarization versus fast direction and delay times for stations within the Sumatran Fault and back-arc regions. Plots suggest a $\pi/2$ periodicity with favorable models suggesting Φ_1, $\delta t_1 = 50°$, 0.06 s and Φ_2, $\delta t_2 = -80°$, 0.06 s (blue line). Models where Φ_1, $\delta t_1 = 50°$, 0.04 s and Φ_2, $\delta t_2 = -80°$, 0.04 s are shown by the red line. The green line is Φ_1, $\delta t_1 = 40°$, 0.06 s and Φ_2, $\delta t_2 = -90°$, 0.06 s, and the purple line is Φ_1, $\delta t_1 = 60°$, 0.06 s and Φ_2, $\delta t_2 = -70°$, 0.06 s. Black circles are our observations.

polarization estimates is dependent on the quality of the splitting result. Only results passing the strict quality controls described above were selected. Plots (Figure 6) of δt and Φ with respect to source polarization direction for stations within the Sumatran Fault and back-arc region show a near $\pi/2$ periodicity, suggesting that two layers of anisotropy are present. Measurements that deviate from the apparent $\pi/2$ periodicity may be attributed to a dipping symmetry axis or laterally varying anisotropy that have not been included in the model [*Savage and Silver*, 1993; *Silver and Savage*, 1994].

[36] The plots of observed fast directions with respect to source polarization direction for the back arc and Sumatran Fault show a significant jump in the fast direction at a source polarization of ~60°–90° and 0°. *Savage and Silver* [1993] suggest that in order to obtain a significant "jump" in the fast direction, the splitting parameters of layers 1 and 2 must fit the following requirements, $\delta t_1 = \delta t_2$ and $30° < |\Phi_2 - \Phi_1| < 60°$ or $120° < |\Phi_2 - \Phi_1| < 150°$, with the "jump" in fast direction versus source polarization and delay time versus source polarization occurring midway between the two fast/slow directions. Using the previously stated criteria, we fit the observed periodicity using a trial and error method. Favorable models that produce a "jump" in the fast direction from −90° to 90° at source polarizations of 0° and 60°–80° suggest a lower layer orientated NE-SW (050° ± 10°) producing delay times of 0.06 s and an upper layer that has a similar delay time but with a fast polarization direction of −080° ± 10° (Figure 6). If the delay time of each layer is reduced to 0.04 s, the modeled cumulative delay times are smaller than the observed (Figure 6, red line), giving us a lower limit on the anisotropy values. The orientation of the lower layer is approximately perpendicular to the strike of the trench (~140°), which is what is expected for 2-D corner flow, and the small delay time agrees with the observations of *Hammond et al.* [2010], suggesting the mantle wedge is only weakly anisotropic. The fast polarization direction of the upper layer of anisotropy, −80°, is oblique to the general trend of the Sumatran Fault (−40° to −50°), but as discussed earlier, the fault is not a simple NW-SE trending structure, as it is composed of numerous segments separated by dilational and contractional step overs, with occasional changes in the trend of the fault [*Sieh and Natawidjaja*, 2000]. The largest such feature is in central Sumatra where the SF partitions into two fault strands up to 35 km apart (Figure 4a) and which is proposed to be a strike-slip duplex system with complex faulting between the main fault branches [*Weller et al.*, 2012]. Furthermore, the fast direction of the upper layer might be influenced by feeder system of the volcanoes located closely to the Sumatran fault. However, the remaining uncertainties of the complex two-layer analysis do not warrant more detailed

interpretation, and further testing of the viability of these or other ideas will require structural analysis beyond the scope of this study.

5.3. Forward Modeling

[37] Synthetic SWS was modeled using the forward modeling software SynthSplit [*Abt and Fischer*, 2008]. SynthSplit predicts SWS parameters using the particle motion perturbation method of *Fischer et al*. [2000] and has been tested with full synthetic waveform methods [*Abt and Fischer*, 2008]. Each anisotropic layer is described by five elastic parameters. The model uses elastic parameters from studies of single crystals and assumes that each aggregate within a defined block of a model is perfectly aligned in the orientation specified. In reality, the observed splitting times are considerably smaller than those predicted from the single crystal elastic coefficients, most likely due to the misalignment of a percentage of the crystals. To simulate this dilution of anisotropy, a dilution factor is introduced. The dilution factor can be calculated using the equation

$$\text{Dilution factor}(‰) = \frac{\text{bulk } S \text{ anisotropy}(‰)}{\text{single crystal anisotropy}(‰)} \times 100,$$

where a single olivine crystal S wave anisotropic strength is 18.1% [*Kumazawa and Anderson*, 1969] and the bulk S anisotropy is the strength of anisotropy within the layer.

[38] SynthSplit was used to model individual events at different stations. SynthSplit only allows one set of elastic parameters to be determined for each model, regardless of the number of layers. For all models, a composition of 70% olivine and 30% orthopyroxene was used and the synthetics were generated using a dominant period of 1.5 s. At crustal depths, olivine-opx elastic coefficient is generally not appropriate, but this composition is used anyway as a proxy for the more likely sources of crustal anisotropy, e.g., stress-induced cracks or deformation fabrics in crustal mineralogies [*Abt and Fischer*, 2008].

[39] The local SWS observations were modeled using two layers of anisotropy. The upper layer is assumed to exhibit a fault-parallel fast polarization direction from the transcurrent motion occurring along the Sumatran Fault so was modeled with the *a* axis orientated NW to SE (−40°), which is the general trend of the Sumatran Fault, dipping at 0°. The lower layer of anisotropy, which originates from 2-D corner flow within the mantle wedge, is modeled with the *a* axis orientated approximately perpendicular to the trench, 050°, and a dilution factor of 13% (equivalent to ~2% bulk S anisotropy). For each model outlined in Tables 2–5, the sensitivity of the theoretical SWS to orthorhombic and hexagonal symmetry was tested. The predicted fast directions of the two symmetries are nearly identical, and the delay time differences between the two are generally small, less than 0.12 s, suggesting that using either symmetry will result in approximately the same predicted SWS parameters. For the analysis, we used models with hexagonal symmetry and focused on modeling stations which have the largest number of splitting observations (stations F70S, A20S, N20S, and N40S; Figure 2).

[40] The modeling results and parameters used can be found in Figure 7 and Tables 2–5. The normalized root mean square misfits (NRMS) between the observed and predicted Φ and δt values for each station are shown in Figure 8. This figure also shows the effect of varying the modeling parameters. At station N40S (Figure 7a and Table 2), in the back arc, the observed fast directions are generally trench perpendicular (with the exception of event 4). The results are best modeled using a 150 km thick layer of anisotropy in the mantle wedge, with a weaker upper layer of anisotropy that has a dilution factor of 40% and is 1–50 km thick. Similar NRMS misfits between the observed and predicted values of Φ are also observed when the thickness of the lower layer is reduced by 20 km (Figure 8a, model 9). The NRMS misfit for δt using the modeling parameters in Table 2 is ~0.4. A lower NRMS misfit for δt is observed when the Φ of the lower layer is changed to 30° (model 7), but a substantially higher NRMS misfit is observed for Φ. At station N20S (Figure 7b and Table 3), which is closer to the Sumatran Fault, station A20S (Figure 7c and Table 4), on the Sumatran

Table 3. Forward Modeling Parameters for Local SWS for Station N20S

Station N20S	Upper Layer (Layer 1)			Lower Layer (Layer 2)		
Event No.	Azimuth (°)	Dilution Factor (%)	Thickness (km)	Azimuth (°)	Dilution Factor (%)	Thickness (km)
1	−40	60	40	50	13	80
2	−40	60	30	50	13	80
3	−40	60	40	50	13	80
4	−40	60	30	50	13	80
5	−40	60	37	50	13	80
6	−40	60	40	50	13	80
7	−40	60	40	50	13	80

Table 2. Forward Modeling Parameters for Local SWS for Station N40S

Station N40S	Upper Layer (Layer 1)			Lower Layer (Layer 2)		
Event No.	Azimuth (°)	Dilution factor (%)	Thickness (km)	Azimuth (°)	Dilution Factor (%)	Thickness (km)
1	−40	40	1	50	13	150
2	−40	40	1	50	13	150
3	−40	40	30	50	13	150
4	−40	40	50	50	13	150
5	−40	40	20	50	13	150
6	−40	40	30	50	13	150

Table 4. Forward Modeling Parameters for Local SWS for Station A20S

Station A20S	Upper Layer (Layer 1)			Lower Layer (Layer 2)		
Event No.	Azimuth (°)	Dilution Factor (%)	Thickness (km)	Azimuth (°)	Dilution Factor (%)	Thickness (km)
1	−40	50	30	50	13	25
2	−40	50	30	50	13	25
3	−40	50	30	50	13	25
4	−40	50	40	50	13	25
5	−40	50	40	50	13	25
6	−40	50	30	50	13	25

Table 5. Forward Modeling Parameters for Local SWS for Station F70S

Station F70S	Upper Layer (Layer 1)			Lower Layer (Layer 2)		
Event No.	Azimuth (°)	Dilution Factor (%)	Thickness (km)	Azimuth (°)	Dilution Factor (%)	Thickness (km)
1	−40	60	20	50	13	25
2	−40	60	20	50	13	25
3	−40	60	30	50	13	25
4	−40	60	25	50	13	25
5	−40	60	20	50	13	25
6	−40	60	25	50	13	25
7	−40	60	25	50	13	25
8	−40	60	20	50	13	25

Fault, and station F70S (Figure 7d and Table 5), west of the Sumatran Fault, the predominant fast direction is trench/fault parallel. The modeling suggests that the lower layer of anisotropy decreases in thickness from 80 km beneath station N20S to 25 km beneath station F70S, implying that the strength of anisotropy in the mantle wedge decreases moving westward from the back arc to the fore arc. Figures 8b–8d suggest that varying the thickness of the lower layer of anisotropy by ±10 km (models 9 and 10) generally does not greatly increase the NRMS misfit for Φ and δt at these three stations. A larger increase in NRMS misfit is observed when Φ of the lower layer is altered to either 30° or 70° (Figures 8b–8d, models 7 and 8). Anisotropy in the upper layer beneath stations N20S, A20S, and F70S is stronger than the lower layer, with a dilution factor and thickness of 50–60% and 20–40 km, respectively, thus causing the observed trench/fault-parallel fast directions. Figures 8b–8d indicate that using an upper layer with Φ of either −80° (model 2) or −20° (model 3) causes the NRMS misfit for Φ and δt to increase substantially at these stations.

[41] The forward modeling results show that the observed fast directions in the Sumatran Fault and back-arc regions can be reproduced by two layers of anisotropy. At stations close to and beneath the Sumatran Fault, the upper layer of anisotropy dominates, resulting in trench/fault-parallel fast directions, while in the back arc, the anisotropy in the lower layer is stronger, causing trench-perpendicular fast directions. These results support our conclusion that the observed splitting from the local *S* waves in the Sumatran Fault region and back arc is due to an upper layer of anisotropy, which has formed from fault-parallel aligned fractures and minerals in the overriding plate, and a lower layer of anisotropy, within the mantle wedge, due to corner flow (Figure 9).

6. Teleseismic Splitting and Possible Mechanisms

[42] Comparing the delay times of the *SKS* SWS measurements to the delay times of the local SWS measurements allows us to constrain where the anisotropy that generates the *SKS* SWS is located. Though the local SWS measurements and *SKS* SWS measurements were filtered using different frequency bands, the filter bands overlap and this should minimize the frequency-dependent effects between the two data sets. The maximum delay time observed from the local SWS observation is 0.42 s, whereas the delay times of the *SKS* SWS measurements are between 0.8 and 3.0 s (Figure 3). As the local SWS results show only a small amount of splitting, most of the anisotropy that causes the observed *SKS* SWS must come from beneath the slab interface.

[43] *Long and Silver*'s [2008] global study of SWS concluded that subwedge splitting is dominated by trench-parallel directions with only a few exceptions (e.g., Cascadia [*Currie et al.*, 2004] and south-central Chile [*Hicks et al.*, 2012]). Generally, teleseismic SWS measurements reported here exhibit a fast direction which is approximately parallel to the motion of the subducting Indo-Australian Plate and does not fit the global trend observed by *Long and Silver* [2008]. The predominantly APM-parallel fast direction agrees with

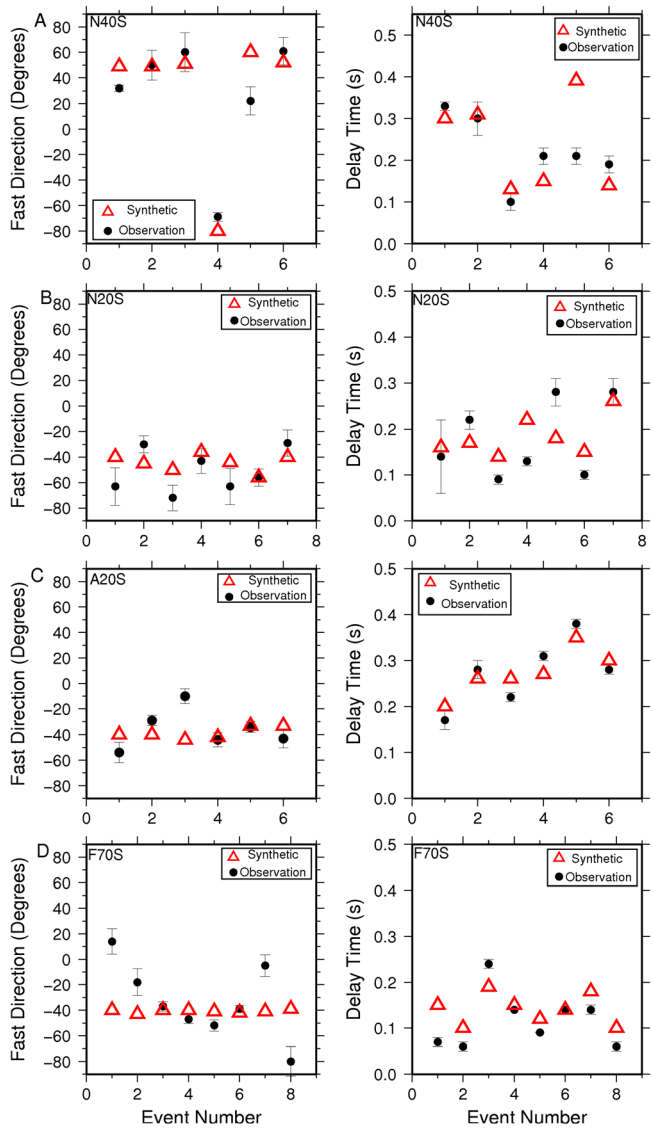

Figure 7. Comparison of predicted and observed local SWS. (a) Station N40S in the back-arc region (see Table 2 for details). (b) Station N20S in the back-arc region (Table 3). (c) Station A20S in the Sumatran Fault region (Table 4). (d) Station F70S in the Sumatran Fault region (Table 5). Black circles are observed splitting parameters. Red triangles are predicted SWS. Station locations are shown in Figure 2.

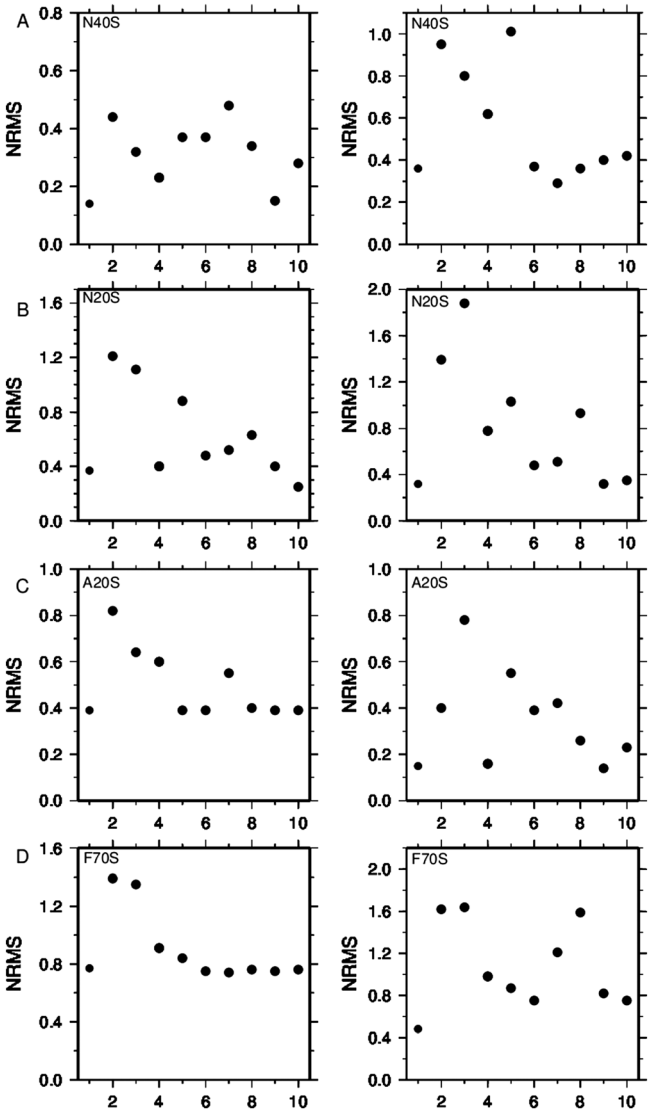

Figure 8. The normalized root mean squared (NRMS) misfit between the observed and predicted Φ (left-hand panel) and δt (right-hand panel) values for stations N40S, N20S, A20S, and F70S using 10 different models. The x axis indicates the model index. Model l uses the parameters stated in Tables 2–5. For the subsequent models, unless otherwise stated, the parameters used in the forward modeling are the same as shown in Tables 2–5. Model 2: Upper layer Φ is $-80°$. Model 3: Upper layer Φ is altered to $-20°$. Model 4: Upper layer Φ is altered to $-60°$s. Model 5: Upper layer thickness is reduced by 10 km. Model 6: Upper layer thickness is increased by 10 km. Model 7: Lower layer Φ is altered to 30°. Model 8: Lower layer Φ is altered to 70°. Model 9: Lower layer thickness is reduced by 10 km for stations N20S, A20S, and F70S and 20 km for N40S. Model 10: Lower layer thickness is increased by 10 km for stations N20S, A20S, and F70S and 20 km for N40S.

Hammond et al. [2010] who attribute their *SKS* SWS observations to fossilized anisotropy within the subducting slab. However, the forward modeling approach of *Hammond et al*. [2010] uses a steeply dipping (>45°) slab, but local seismicity [*Lange et al*., 2010; *Collings et al*., 2012] clearly indicates a shallower dipping slab for the region (~35° until 100 km depth) which causes the rays to travel predominantly in the oceanic asthenosphere, not within the lithosphere of the subducting slab. Additionally, the thickness of the lithosphere in their model is estimated to be 100 km beneath both Sumatra and Java which ignores the significant difference in slab age between these two regions (49 Ma below North Sumatra, where the Wharton Fossil Ridge subducts, to 134 Ma beneath Java) and is unrealistically large for Sumatra. So, although fossilized anisotropy within the subducting slab may contribute to the splitting, another source is likely to be present.

[44] Preferentially orientated hydrated faults and cracks within the uppermost slab have been shown to cause strong SWS with trench-parallel fast directions [*Faccenda et al*., 2008; *Healy et al*., 2009]. Previous bathymetry, seismic reflection, gravity, and magnetic surveys [*Deplus et al*., 1998; *Graindorge et al*., 2008] in the Sunda Arc have found that the subducting Indo-Australian Plate south of Sumatra has N-S trending faults, approximately parallel to the convergence direction, while at Java, trench-parallel (~E-W) normal faults are present on the oceanic crust adjacent to the trench [*Masson et al*., 1990], therefore reflecting the observed rotation in the fast direction of the *SKS* measurements. Despite this, previous modeling results by *Hammond et al*. [2010] show that a thin anisotropic layer at the top of the slab cannot fit their observations as the rays only spend a small amount of time within this layer.

[45] The alignment of the *SKS* fast directions with the direction of motion of the Indo-Australian Plate suggests that anisotropy is caused by entrained flow of the asthenosphere beneath the subducting slab. This was first suggested by *Savage* [1999] who concluded that when a subducting slab is moving over relatively stable asthenosphere, the *a* axis and therefore the fast directions are orientated parallel to the direction of plate motion. However, due to the number of trench-parallel observations being recorded from teleseismic phases, this model was discounted for most subduction zones [*Long and Silver*, 2008]. Numerical modeling of entrained asthenospheric flow by *Morgan et al*. [2007] suggests that the lower side of the slab entrains a layer of asthenosphere, whose thickness depends upon the subduction rate, density contrast, and viscosity of the asthenosphere. When the asthenosphere has a 200 km thick upper layer that has a higher temperature and is more depleted than the underlying mantle (formed by buoyant upwelling plumes), a thin sheet (10–30 km thick) of asthenosphere is entrained by the subducting slab and a large scale return flow away from the trench occurs. The thickness of the entrained sheet increases as the subduction rate increases and will be thicker beneath the fore arc than beneath the back arc. However, when there is no strong density and viscosity contrast in the upper asthenosphere layer, the asthenosphere is easily dragged down by the slab, resulting in a thick layer (up to 200 km) of asthenosphere being entrained by the slab [*Morgan et al*., 2007]. As the asthenosphere is dragged down beneath the slab, simple shear causes the LPO of minerals (predominantly olivine), with the *a* axis dipping approximately at the same angle as the slab and pointing along the convergence direction. This would result in a significant layer of anisotropy beneath the subducting slab.

[46] Trench-parallel directions exhibited by teleseismic phases at the majority of subduction zones around the world

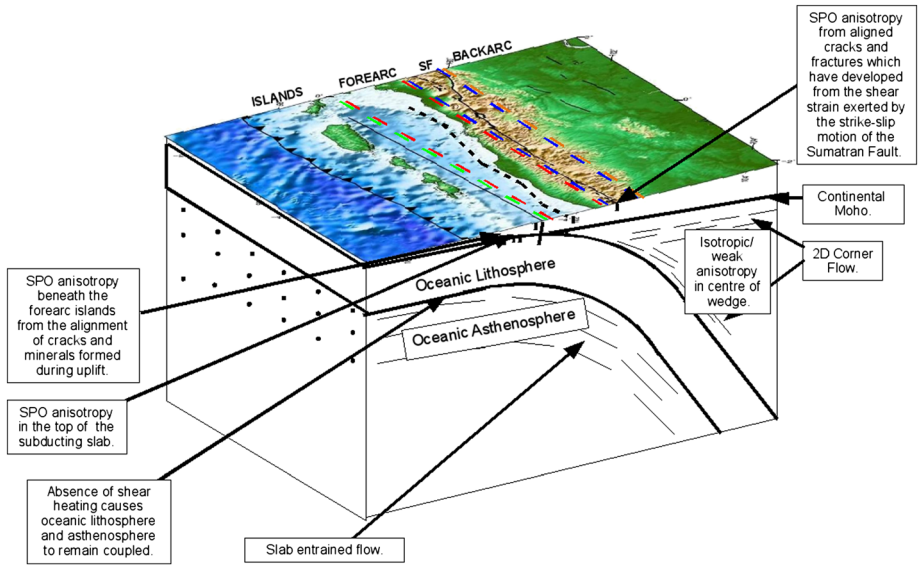

Figure 9. Figure illustrating the different types of anisotropy observed along the Sumatran Margin.

are attributed to trench-parallel flow induced by trench migration and require decoupling between the slab and asthenosphere, a partial barrier to flow at depths and a distant barrier to horizontal flow [*Long and Silver*, 2008]. It is possible that these requirements are not being fulfilled in some subduction zones, including Sumatra, Cascadia, and south-central Chile. *Long and Silver* [2009] hypothesize for Cascadia, where the teleseismic SWS observations exhibit trench-perpendicular splitting [*Currie et al*., 2004] despite ongoing trench migration, that the mechanism for decoupling is not working properly. They propose that the decoupling between the slab and asthenosphere occurs due to a thin entrained layer of hot asthenosphere [*Morgan et al*., 2007], which requires an upper asthenosphere that is physically distinct from its surroundings. However, unlike *Morgan et al*. [2007], this physically distinct layer is not attributed to buoyant mantle upwelling; instead, it is thought to be a result of shear heating [*Long and Silver*, 2009]. Shear heating occurs when mantle material beneath newly formed lithosphere is subjected to shear deformation by the motion of the overlying oceanic plate as it moves away from the ridge. Beneath Cascadia, it is thought that the young lithosphere (5–10 Ma) has not reached the amount of strain needed for the shear heating mechanism to produce the very low viscosities needed for decoupling the motion of the slab from the surrounding asthenosphere, allowing a thick layer of asthenosphere to be easily entrained by the slab [*Morgan et al*., 2007]. If this hypothesis is true, one would expect to observe APM-parallel fast directions at other subduction zones where young lithosphere is subducting and a transition in fast direction from APM parallel to trench parallel in subduction zones where there is an along-strike increase in the age of the subducting crust. Beneath northern Sumatra (where the Wharton Fossil Ridge subducts) and Java, there is such an along-strike age variation from 49 Ma in North Sumatra to 134 Ma in Java (Figure 1). Although the Indo-Australian subducting under Sumatra plate is significantly older than in Cascadia, one would still expect the coupling between the asthenosphere and overlying lithosphere to be stronger beneath northern Sumatra than beneath Java as the amount of shear strain that has been induced will be smaller. The reduced strain beneath Sumatra may therefore not have reached the amount needed for the shear heating mechanism to reach a steady state, allowing the entrainment of the subslab asthenosphere. A similar observation of *SKS* SWS fast directions parallel to plate convergence direction has been made in south-central Chile, where the plate age is 30 Ma [*Hicks et al*., 2012].

[47] Another important difference between Java and Sumatra is the transition from normal subduction to oblique subduction (Figure 1). Could the change in geometry be responsible for the trench-parallel flow observed beneath Java and trench-oblique flow seen beneath Sumatra? The slab between Java and Sumatra appears continuous [*Syracuse and Abers*, 2006], and despite the change in subduction angle, both regions are undergoing similar magnitudes of trench advance [*Lallemand et al*., 2008], suggesting that lateral flow should be able to develop beneath Java and Sumatra. This, along with the observation of trench-parallel splitting from subslab anisotropy at other oblique subduction zones [e.g., New Zealand, *Marson-Pidgeon et al*., 1999], leads us to reject the transition from normal to oblique subduction as the cause of the different subslab flows observed between Java and Sumatra.

[48] Trench-perpendicular fast directions are observed at three stations situated on Batu and Nias Island (blue lines, Figure 3), similar to the SKS measurements observed at Nias Island by *Hammond et al*. [2010]. Though the measurements were not classified as good because the delay time ratio of the splitting parameters obtained using the rotation correlation method and minimum transverse energy method were not between 0.7 and 1.2 and the misfit between the fast directions was greater than 15°, the results were stable in the three different SWS analysis techniques and therefore should not be automatically rejected. A possible explanation for the small area of trench-perpendicular fast directions is that in this region of the subduction zone, the investigator fracture zone is subducting beneath the Eurasian plate, which may complicate the anisotropy.

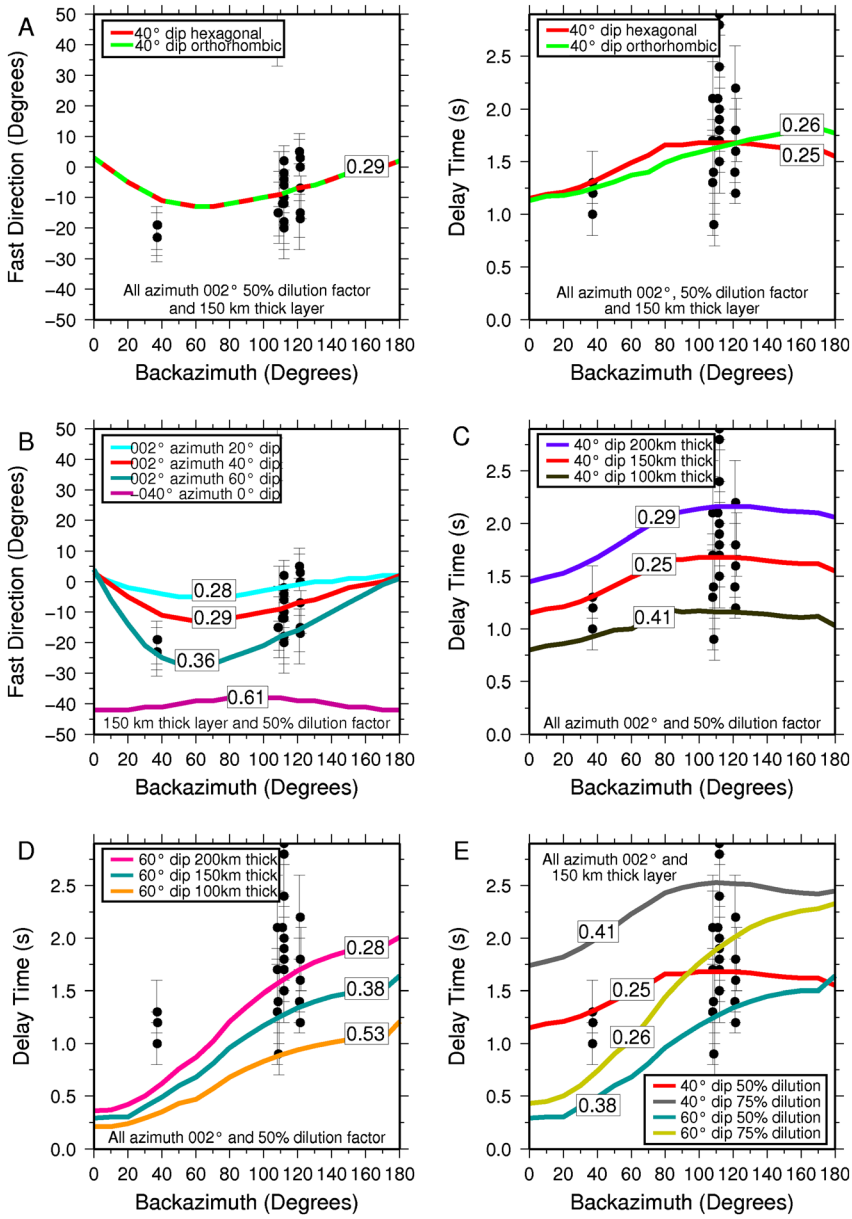

Figure 10. Comparison of predicted and observed teleseismic SWS (black circles). Unless otherwise stated, the parameters used in the forward modeling are as follows: 150 km thick layer, 50% dilution factor, *a* axis azimuth 002°, and its dip 40° assuming hexagonal symmetry. (a) Effect of symmetry axis on predicted SWS. (b) Sensitivity of predicted SWS to *a* axis dip. (c) Sensitivity of predicted SWS to layer thickness with an *a* axis dipping at 40°. (d) Sensitivity of predicted SWS to layer thickness with an *a* axis dipping at 60°. (e) Sensitivity of predicted SWS to dilution factor and *a* axis dip.

[49] From the above discussion, we suggest that the observed teleseismic SWS is likely to be dominated by LPO subslab anisotropy that has developed due to a thick layer of asthenosphere being entrained by the subducting slab (Figure 9). A possible mechanism for entrained flow and not trench-parallel flow is that despite ongoing trench advance, the shear heating mechanism thought to be responsible for decoupling at most subduction zones has not yet produced a low-viscosity layer, such that the subducting lithosphere and underlying asthenosphere remain coupled. As the fossil spreading direction is almost parallel to the absolute plate motion, it is possible that it also contributes to the observed splitting, but the thickness of the lithosphere is far too small to account for the observed splitting delay times.

6.1. Forward Modeling

[50] Similar to the local SWS observations, SynthSplit [*Abt and Fischer*, 2008] was used to forward model the teleseismic SWS observations. For all models, a single layer composed of 70% olivine and 30% orthopyroxene was used to represent the subslab anisotropic layer. The synthetics were generated using a period of 6.5 s (~0.15 Hz), a typical frequency of the *SKS* waves. We performed numerous sensitivity tests comparing theoretical and observed SWS

for each of the input parameters provided by SynthSplit. In particular, we tested the orientation (azimuth) and dip (20°–60°) of the *a* axis, symmetry, thickness, and dilution factor. Predicted fast directions for hexagonal and orthorhombic symmetries are typically nearly identical (Figure 10a). The NRMS misfit for both cases is 0.29. The delay times between the two symmetries vary with backazimuth, but generally, the differences are small, less than 0.25 s, and the NRMS misfit varies by 0.01 (Figure 10a).

[51] The fast directions were modeled using *a* axes orientated at different azimuths and dip. When the *a* axis is orientated parallel to the trench (−040º), the predicted fast directions clearly do not fit the observed SWS observations (Figure 10b). The NRMS misfit is 0.61. The observed fast direction are best modeled by a layer that has its *a* axis aligned in the absolute direction of plate motion (~002°) [*Prawirodirdjo et al*., 2000] and dipping steeply at 40°–60°, steeper than the dip of the plate (~35°).

[52] In order to model the observed delay times, the dilution factor and thickness of the layers were varied. For *a* axis dips of 40° and 60°, models were run with layers 100, 150, and 200 km thick and dilution factors of 50% and 75% (Figures 10c–10e). There is a strong trade-off between the layer thickness and the dilution factor as a thicker layer and higher dilution factor will result in larger delay times. A layer whose *a* axis is dipping at 60° with either a thick layer (>200 km when a dilution factor of 50% is used) or a high dilution factor (>75%, with a 150 km thick layer) fits the observed delay times for backazimuths of 100°–120° but is unable to fit the observed delay times for backazimuths of ~37°. However, if the *a* axis is dipping at 40°, a layer 150 km thick with a dilution factor of 50–75% can model all the observed delay times reasonably well. The actual anisotropic strength is likely to be smaller, as we have not included the splitting accrued in the slab, mantle wedge, and crust, which will contribute to the observed delay times.

[53] The forward modeling shows that the *SKS* SWS fast direction/delay time dependency on backazimuth can be modeled using a thick (150–200 km) layer of strong anisotropy (~9% bulk *S* anisotropy) that has its *a* axis aligned with the convergence direction (~002°). Furthermore, the forward modeling results suggest that the fast direction dependency on backazimuth is best modeled using an *a* axis which is dipping steeply at 40°–60°. However, the forward modeling of the delay time dependency on backazimuth suggests that an *a* axis dip of 60° is unable to fit all the observations. The delay times are best modeled using an *a* axis dip of ~40°. A dip of 40° is similar to the dip of the subducting slab (~35°) at 40–100 km depth [*Collings et al*., 2012]. However, these values are likely to be poorly constrained due to the simplicity of the forward modeling; for example, it has been assumed that all of the rays arrive at an incidence angle of 10° and the *a* axis dip is constant. Despite this, the modeling results suggest that the observed teleseismic SWS is from the LPO subslab anisotropy that has developed due to a thick layer of asthenosphere being entrained by the subducting slab (Figure 9).

7. Conclusions

[54] Using local seismic data from two temporary seismic networks in the Sumatra subduction zone, we have used SWS observations to improve our understanding of the style and geometry of deformation that occurs. Our main findings are as follows (Figure 9):

[55] 1. Beneath the fore-arc islands, which are located 75–150 km from the deformation front, a layer of SPO anisotropy is located within the low-velocity sediments due to the alignment of cracks and fractures that were formed when the sediments were uplifted.

[56] 2. In the Sumatran Fault region, the predominant fast direction of local earthquake SWS is trench/fault parallel. The trench/fault-parallel fast direction is attributed to a layer of anisotropy in the continental lithosphere. The anisotropy is formed by fault-parallel aligned minerals and fractures that have developed from the shear strain exerted by the strike-slip motion of the Sumatran Fault. In order to explain all of the measurements within the back arc, the anisotropic layer has to be confined to a ~100 km region around the fault.

[57] 3. In the back-arc region, the predominant fast direction of local earthquake SWS is trench perpendicular. The observed SWS is attributed to LPO anisotropy in the mantle wedge due to 2-D corner flow. The small delay times suggest that the center of the mantle wedge either is isotropic or contains weak anisotropy.

[58] 4. *SKS* SWS is primarily sensitive to the subslab anisotropy structure and indicates that, beneath the slab interface, a thick layer (150–200 km) of LPO anisotropy has developed due to the asthenosphere being entrained by the subducting slab. The *a* axis of the olivine crystals is aligned parallel to the APM direction of the Indo-Australian Plate and is at a similar dip (~40°) to the dip of the subducting slab (35°). A possible mechanism for the oceanic lithosphere and asthenosphere to remain coupled is that the shear heating mechanism has not yet heated up the boundary layer below the slab sufficiently to allow a very low viscosity channel to form and cause decoupling between the subducting plate and the asthenosphere.

[59] **Acknowledgments.** The project was funded by NERC (NE/D002575/1 and NE/F012209/1). We thank the SeisUK facility in Leicester (loans 828 and 858) and the University of Liverpool for the provision of instruments. We also thank the Earth Observatory Singapore for funding part of the fieldwork and letting us co-occupy sites of the SuGAr GPS array. We acknowledge the support of colleagues at Geotek-LIPI and the whole field crew which made this experiment possible. We gratefully acknowledge the cooperation of many Sumatran landowners for allowing us to install the seismic stations on their property. Furthermore, we thank the captain and crew of the Andalas and the field crews for their excellent work under difficult conditions.

References

Abt, D. L., and K. M. Fischer (2008), Resolving three-dimensional anisotropic structure with shear wave splitting tomography, *Geophys. J. Int.*, *173*(3), 859–886, doi:10.1111/j.1365-246X.2008.03757.X.

Abt, D. L., K. M. Fischer, G. A. Abers, W. Strauch, J. M. Protti, and V. Gonzalez (2009), Shear wave anisotropy beneath Nicaragua and Costa Rica: Implications for flow in the mantle wedge, *Geochem. Geophys. Geosyst.*, *10*, doi:10.1029/2009GC002375.

Alsina, D., and R. Snieder (1995), Small-scale sub-lithospheric continental mantle deformation: Constraints from SKS splitting observations, *Geophys. J. Int.*, *123*, 431–448, doi:10.1111/j.1365-246X.1995.tb06864.x.

Ando, M., Y. Ishikawa, and F. Yamazaki (1983), Shear Wave Polarization in the upper mantle beneath Honshu, Japan, *J. Geophys. Res.*, *88*(7), 5850–5864, doi:10.1029/JB088iB07p05850.

Audoine, E., M. K. Savage, and K. Gledhill (2000), Seismic anisotropy from local earthquakes in the transition region from a subduction to a strike-slip plate boundary, New Zealand, *J. Geophys. Res.*, *105*(B4), 8013–8033, doi:10.1029/1999JB900444.

Audoine, E., M. K. Savage, and K. Gledhill (2004), Anisotropic structure under a back-arc spreading region, the Taupo Volcanic Zone, New Zealand, *J. Geophys. Res.*, *109*, B11305, doi:10.1029/2003JB002932.

Babuška, V., and M. Cara (1991), *Seismic anisotropy in the Earth*, Kluwer Acad. Pub., Dordrecht, The Netherlands.

Backus, G. E. (1962), Long-wave elastic anisotropy produced by horizontal layering, *J. Geophys. Res.*, *67*(11), 4427, doi:10.1029/JZ067i011p04427.

Balfour, N. J., M. K. Savage, and J. Townend (2005), Stress and crustal anisotropy in Marlborough, New Zealand: Evidence for low fault strength and structure-controlled anisotropy, *Geophys. J. Int.*, *163*(3), 1073–1086, doi:10.1111/j.1365-246X.2005.02783.X.

Bowman, J. R., and M. Ando (1987), Shear-wave splitting in the upper mantle wedge above the Tonga subduction zone, *Geophys. J. R. Astron. Soc.*, *88*(1), 25–41, doi:10.1111/j.1365-246X.1987.tb01367.X.

Christensen, N. I. (1984), The magnitude, symmetry and origin of upper mantle anisotropy based on fabric analyses of ultramafic tectonites, *Geophys. J. Int.*, *76*(1), 89–111, doi:10.1111/j.1365-246X.1984.tb05025.X.

Collings, R., D. Lange, F. Tilmann, A. Rietbrock, D. H. Natawidjaja, B. Suwargadi, M. Miller, and J. Saul (2012), Structure and seismogenic properties of the Mentawai segment of the Sumatra subduction zone revealed by local earthquake travel time tomography, *J. Geophys. Res.*, *117*(B01312), doi:10.1029/2011JB008469.

Crampin, S. (1994), The fracture criticality of crustal rocks, *Geophys. J. Int.*, *118*(2), 428–438, doi:10.1111/j.1365-246X.1994.tb03974.X.

Crampin, S., T. Volti, S. Chastin, A. Gudmundsson, and R. Stefansson (2002), Indication of high pore-fluid pressures in a seismically-active fault zone, *Geophys. J. Int.*, *151*(2), F1–F5, doi:10.1046/j.1365-246X.2002.01830.X.

Currie, C. A., J. F. Cassidy, R. D. Hyndman, and M. G. Bostock (2004), Shear wave anisotropy beneath the Cascadia subduction zone and western North American craton, *Geophys. J. Int.*, *157*(1), 341–353, doi:10.1111/j.1365-246X.2004.02175.X.

Deplus, C., M. Diament, H. Hébert, G. Bertrand, S. Dominguez, J. Dubois, J. Malod, P. Patriat, B. Pontoise, and J. J. Sibilla (1998), Direct evidence of active deformation in the eastern Indian oceanic plate, *Geology*, *26*(2), 131–134.

Diament, M., H. Harjono, K. Karta, C. Deplus, M. Gerard, O. Lassal, A. Martin, and J. Malod (1992), Mentawai Fault zone off Sumatra—A new key to the geodynamics of western Indonesia, *Geology*, *20*(3), 259–262,

Evans, R. (1984), Effects of the free-surface on shear wavetrains, *Geophys. J. R. Astron. Soc.*, *76*(1), 165–172, doi:10.1111/j.1365-246X.1984.tb05032.X.

Faccenda, M., L. Burlini, T. V. Gerya, and D. Mainprice (2008), Fault-induced seismic anisotropy by hydration in subducting oceanic plates, *Nature*, *455*(7216), 1097, doi:10.1038/nature07376.

Fischer, K. M., E. M. Parmentier, A. R. Stine, and E. R. Wolf (2000), Modeling anisotropy and plate-driven flow in the Tonga subduction zone back arc, *J. Geophys. Res.*, *105*(B7), 16,181–16,191, doi:10.1029/1999JB900441.

Fukao, Y. (1984), Evidence from core-reflected shear-waves for anisotropy in the earth's mantle, *Nature*, *309*(5970), 695–698, doi:10.1038/309695a0.

Gledhill, K. R., and G. Stuart (1996), Seismic anisotropy in the fore-arc region of the Hikurangi subduction zone, New Zealand, *Phys. Earth Planet. Inter.*, *95*, 211–225, doi:10.1016/0031-9201(95)03117-0.

Graindorge, D., et al. (2008), Impact of lower plate structure on upper plate deformation at the NW Sumatran convergent margin from seafloor morphology, *Earth Planet. Sci. Lett.*, *275*(3–4), 201–210, doi:10.1016/j.epsl.2008.04.053.

Greve, S. M., M. K. Savage, and S. D. Hofmann (2008), Strong variations in seismic anisotropy across the Hikurangi subduction zone, North Island, New Zealand, *Tectonophysics*, *462*(1–4), 7–21, doi:10.1016/j.tecto.2007.07.011.

Hall, C. E., K. M. Fischer, E. M. Parmentier, and D. K. Blackman (2000), The influence of plate motions on three-dimensional back arc mantle flow and shear wave splitting, *J. Geophys. Res.*, *105*(B12), 28,009–28,033, doi:10.1029/2000JB900297.

Hammond, J. O. S., J. Wookey, S. Kaneshima, H. Inoue, T. Yamashina, and P. Harjadi (2010), Systematic variation in anisotropy beneath the mantle wedge in the Java-Sumatra subduction system from shear-wave splitting, *Phys. Earth Planet. Inter.*, *178*(3–4), 189–201, doi:10.1016/j.pepi.2009.10.003.

Harmon, N., D. W. Forsyth, K. M. Fischer, and S. C. Webb (2004), Variations in shear-wave splitting in young Pacific seafloor, *Geophys. Res. Lett.*, *31*, doi:10.1029/2004GL020495.

Hayes, G. P., and D. J. Wald (2009), Developing framework to constrain the geometry of the seismic rupture plane of the subduction interface a prior—A probabilistic approach, *Geophys. J. Int.*, *176*, 951–964, doi:10.1111/j.1365-246X.2008.04035.X.

Healy, D., S. M. Reddy, N. E. Timms, E. M. Gray, and A. V. Brovarone (2009), Trench-parallel fast axes of seismic anisotropy due to fluid-filled cracks in subducting slabs, *Earth Planet. Sci. Lett.*, *283*(1–4), 75–86.

Hicks, S. P., S. E. J. Nippress, and A. Rietbrock (2012), Sub-slab mantle anisotropy beneath south-central Chile, *Earth Planet. Sci. Lett.*, *357–358*, 203–213, doi:10.1016/j.epsl.2012.09.017.

Hoernle, K., et al. (2008), Arc-parallel flow in the mantle wedge beneath Costa Rica and Nicaragua, *Nature*, *451*(7182), 1094, doi:10.1038/nature06550.

Honda, S., and T. Yoshida (2005), Effects of oblique subduction on the 3-D pattern of small-scale convection within the mantle wedge, *Geophys. Res. Lett.*, *32*, doi:10.1029/2005GL023106.

Huang, Z., D. Zhao, and L. Wang (2011), Shear wave anisotropy in the crust, mantle wedge, and subducting Pacific slab under northeast Japan, *Geochem. Geophys. Geosyst.*, *12*, doi:10.1029/2010GC003343.

Jung, H., and S. Karato (2001), Water-induced fabric transitions in olivine, *Science*, *293*(5534), 1460–1463, doi:10.1126/science.1062235.

Jung, H., I. Katayama, Z. Jiang, T. Hiraga, and S. Karato (2006), Effect of water and stress on the lattice-preferred orientation of olivine, *Tectonophysics*, *421*(1–2), 1–22, doi:10.1016/j.tecto.2006.02.011.

Jung, H., W. Mo, and H. W. Green (2009), Upper mantle seismic anisotropy resulting from pressure-induced slip transition in olivine, *Nat. Geosci.*, *2*(1), 73–77, doi:10.1038/ngeo389.

Kaneshima, S. (1990), Origin of crustal anisotropy—Shear-wave splitting studies in Japan, *J. Geophys. Res.*, *95*(B7), 11,121–11,133, doi:10.1029/JB095iB07p11121.

Katayama, I., H. Jung, and S. I. Karato (2004), New type of olivine fabric from deformation experiments at modest water content and low stress, *Geology*, *32*(12), 1045–1048.

Katayama, I., and S. I. Karato (2006), Effect of temperature on the B- to C-type olivine fabric transition and implication for flow pattern in subduction zones, *Phys. Earth Planet. Inter.*, *157*(1–2), 33–45, doi:10.1016/j.pepi.2006.03.005.

Klosko, E. R., F. T. Wu, H. J. Anderson, D. Eberhart-Phillips, T. V. McEvilly, E. Audoine, M. K. Savage, and K. R. Gledhill (1999), Upper mantle anisotropy in the New Zealand Region, *Geophys. Res. Lett.*, *26*(10), 1497–1500, doi:10.1029/1999GL900273.

Kopp, H., E. R. Flueh, D. Klaeschen, J. Bialas, and C. Reichert (2001), Crustal structure of the central Sunda margin at the onset of oblique subduction, *Geophys. J. Int.*, *147*(2), 449–474, doi:10.1046/j.0956-540x.2001.01547.X.

Krumbein, W. C. (1939), Preferred orientation of pebbles in sedimentary deposits, *J. Geol.*, *47*(7), 673–706.

Kubo, A., and Y. Hiramatsu (1998), On presence of seismic anisotropy in the asthenosphere beneath continents and its dependence on plate velocity: Significance of reference frame selection, *Pure Appl. Geophys.*, *151*(2–4), 281–303, doi:10.1007/s000240050115.

Kumazawa, M., and O. L. Anderson (1969), Elastic moduli, pressure derivatives, and temperature derivatives of single-crystal olivine and single-crystal forsterite, *J. Geophys. Res.*, *74*(25), 5691–5972, doi:10.1029/JB074i025p05961.

Lallemand, S., A. Heuret, C. Faccenna, and F. Funiciello (2008), Subduction dynamics as revealed by trench migration, *Tectonics*, *27*(3), doi:10.1029/2007TC002212.

Lange, D., F. Tilmann, A. Rietbrock, R. Collings, D. H. Natawidjaja, B. W. Suwargadi, P. Barton, T. Henstock, and T. Ryberg (2010), The fine structure of the subducted investigator fracture zone in western Sumatra as seen by local seismicity, *Earth Planet. Sci. Lett.*, *298*(1–2), 47–56, doi:10.1016/j.epsl.2010.07.020.

Lassak, T. M., M. J. Fouch, C. E. Hall, and E. Kaminski (2006), Seismic characterization of mantle flow in subduction systems: Can we resolve a hydrated mantle wedge?, *Earth Planet. Sci. Lett.*, *243*(3–4), 632–649, doi:10.1016/j.epsl.2006.01.022.

Levin, V., D. Droznin, J. Park, and E. Gordeev (2004), Detailed mapping of seismic anisotropy with local shear waves in southeastern Kamchatka, *Geophys. J. Int.*, *158*(3), 1009–1023, doi:10.1111/j.1365-246X.2004.02352.X.

Liu, Y., H. Zhang, C. Thurber, and S. Roecker (2008), Shear wave anisotropy in the crust around the San Andreas Fault near Parkfield: Spatial and temporal analysis, *Geophys. J. Int.*, *172*(3), 957–970, doi:10.1111/j.1365-246X.2007.03618.X.

Long, M. D., and R. D. van der Hilst (2005), Estimating shear-wave splitting parameters from broadband recordings in Japan: A comparison of three methods, *Bull. Seismol. Soc. Am.*, *95*(4), 1346–1358, doi:10.1785/0120040107.

Long, M. D., and R. D. van der Hilst (2006), Shear wave splitting from local events beneath the Ryukyu arc: Trench-parallel anisotropy in the mantle wedge, *Phys. Earth Planet. Inter.*, *155*(3–4), 300–312, doi:10.1016/j.pepi.2006.01.003.

Long, M. D., and P. G. Silver (2008), The subduction zone flow field from seismic anisotropy: A global view, *Science*, *319*(5861), 315–318, doi:10.1126/science.1150809.

Long, M. D., and P. G. Silver (2009), Mantle flow in subduction systems: The subslab flow field and implications for mantle dynamics, *J. Geophys. Res.*, *114*, doi:10.1029/2008JB006200.

Mainprice, D., G. Barruol, and W. B. Ismail (2000), The seismic anisotropy of the Earth's mantle: From single crystal to polycrystal, in *Earth's Deep Interior, Mineral Physics and Tomography From the Atomic to the Global Scale*, edited by S.-I. Karato, A. M. Forte, R. C. Liberman, G. Masters, and L. Stixrude, AGU, Washington, D. C.

Mainprice, D. (2007), Seismic anisotropy of the deep Earth from a mineral and rock physics perspective, in *Treatise in Geophysics*, vol. 2, edited by G. Schubert, pp. 437–492, Elsevier, Ltd., Oxford, U.K.

Marson-Pidgeon, K., M. K. Savage, K. Gledhill, and G. Stuart (1999), Seismic anisotropy beneath the lower half of the North Island, New Zealand, *J. Geophys. Res.*, *104*(B9), 20,277–20,286, doi:10.1029/1999JB900212.

Masson, D. G., L. M. Parson, J. Milsom, G. Nichols, N. Sikumbang, B. Dwiyanto, and H. Kallagher (1990), Subduction of seamounts at the Java trench—A view with long range sidescan sonar, *Tectonophysics*, *185*(1–2), 51–65, doi:10.1016/0040-1951(90)90404-V.

Morgan, J. P., J. Hasenclever, M. Hort, L. Ruepke, and E. M. Parmentier (2007), On subducting slab entrainment of buoyant asthenosphere, *Terra Nova*, *19*(3), 167–173, doi:10.1111/j.1365-3121.2007.00737.x.

Mount, V. S., and J. Suppe (1992), Present-day stress orientations adjacent to active strike-slip faults, *J. Geophys. Res.*, *97*(B8), 11,995–12,013, doi:10.1029/92JB00130.

Müller, R. D., W. R. Roest, J. Y. Royer, L. M. Gahagan, and J. G. Sclater (1997), Digital isochrons of the world's ocean floor, *J. Geophys. Res.*, *102*(B2), 3211–3214, doi:10.1029/96JB01781.

Nakajima, J., J. Shimizu, S. Hori, and A. Hasegawa (2006), Shear-wave splitting beneath the southwestern Kurile arc and northeastern Japan arc: A new insight into mantle return flow, *Geophys. Res. Lett.*, *33*, doi:10.1029/2005GL025053.

Nicolas, A., and N. I. Christensen (1987), Formation of anisotropy in upper mantle peridotites—A review, in *Composition, Structure and Dynamics of Lithosphere-Asthenosphere System*, Geodynamics, series 16, edited by L. E. Fuch, and C. Froidevaux, AGU, Washington, D. C.

Nippress, S. E. J., N. J. Kusznir, and J. M. Kendall (2007), LPO predicted seismic anisotropy beneath a simple model of a mid-ocean ridge, *Geophys. Res. Lett.*, *34*, doi:10.1029/2006GL029040.

Özalaybey, S., and M. K. Savage (1995), Shear-wave splitting beneath western United-States in relation to plate tectonics, *J. Geophys. Res.*, *100*(B9), 18,135–18,149, doi:10.1029/95JB00715.

Pozgay, S., D. Wiens, J. Conder, H. Shiobara, and H. Sugioka (2007), Complex mantle flow in the Mariana subduction system: Evidence from shear wave splitting, *Geophys. J. Int.*, *170*, 371–386, doi:10.1111/j.1365-246X.2007.03433.x.

Prawirodirdjo, L., Y. Bock, J. F. Genrich, S. S. O. Puntodewo, J. Rais, C. Subarya, and S. Sutisna (2000), One century of tectonic deformation along the Sumatran fault from triangulation and Global Positioning System surveys, *J. Geophys. Res.*, *105*(B12), 28,343–28,361, doi:10.1029/2000JB900150.

Ribe, N. M. (1989), Seismic anisotropy and mantle flow, *J. Geophys. Res.*, *94*(B4), 4213–4223, doi:10.1029/JB094iB04p04213.

Savage, M. K., and P. G. Silver (1993), Mantle deformation and tectonics—Constraints from seismic anisotropy in the western United States, *Phys. Earth Planet. Inter.*, *78*(3–4), 207–227, doi:10.1016/0031-9201(93)90156-4.

Savage, M. K. (1999), Seismic anisotropy and mantle deformation: What have we learned from shear wave splitting?, *Rev. Geophys.*, *37*(1), 65–106, doi:10.1029/98RG02075.

Savage, M. K., K. M. Fischer, and C. E. Hall (2004), Strain modeling, seismic anisotropy and coupling at strike-slip boundaries: Applications in New Zealand and the San Andreas fault, in *Vertical Coupling and Decoupling in the Lithosphere*, vol. 227, edited by J. Grocott, B. Tikoff, K. J. W. McCaffrey, and G. Taylor, pp. 9–40, Geological Society of London, Special Publications, London, U.K.

Shapiro, N. M., M. H. Ritzwoller, and E. R. Engdahl (2008), Structural context of the great Sumatra-Andaman Islands earthquake, *Geophys. Res. Lett.*, *35*, 5, doi:10.1029/2008GL033381.

Sheriff, R. E., and L. P. Geldart (1995), *Exploration Seismology*, Cambridge Univ. Press, Cambridge, U.K.

Sieh, K., and D. Natawidjaja (2000), Neotectonics of the Sumatran fault, Indonesia, *J. Geophys. Res.*, *105*(B12), 28,295–28,326, doi:10.1029/2000JB900120.

Silver, P. G., and W. W. Chan (1988), Implications for continental structure and evolution from seismic anisotropy, *Nature*, *335*, 34–89, doi:10.1038/335034a0.

Silver, P. G., and W. W. Chan (1991), Shear-wave splitting and subcontinental mantle deformation, *J. Geophys. Res.*, *96*(B10), 16,429–16,454, doi:10.1029/91JB00899.

Silver, P. G., and M. K. Savage (1994), The interpretation of shear-wave splitting parameters in the presence of 2 anisotropic layers, *Geophys. J. Int.*, *119*(3), 949–963, doi:10.1111/j.1365-246X.1994.tb04027.x.

Smith, G. P., D. A. Wiens, K. M. Fischer, L. M. Dorman, S. C. Webb, and J. A. Hildebrand (2001), A complex pattern of mantle flow in the Lau backarc, *Science*, *292*(5517), 713–716, doi:10.1126/science.1058763.

Syracuse, E. M., and G. A. Abers (2006), Global compilation of variations in slab depth beneath arc volcanoes and implications, *Geochem. Geophys. Geosyst.*, *7*, doi:10.1029/2005GC001045.

Teanby, N. A., J. M. Kendall, and M. Van der Baan (2004), Automation of shear-wave splitting measurements using cluster analysis, *Bull. Seismol. Soc. Am.*, *94*(2), 453–463, doi:10.1785/0120030123.

Tingay, M., C. Morley, R. King, R. Hillis, D. Coblentz, and R. Hall (2010), Present-day stress field of Southeast Asia, *Tectonophysics*, *482*(1–4), 92–104, doi:10.1016/j.tecto.2009.06.019.

Tono, Y., Y. Fukao, T. Kunugi, and S. Tsuboi (2009), Seismic anisotropy of the Pacific slab and mantle wedge beneath the Japanese islands, *J. Geophys. Res.*, *114*, doi:10.1029/2009JB006290.

Vinnik, L. P., V. Farra, and B. Romanowicz (1989), Azimuthal anisotropy in the earth from observations of SKS at GEOSCOPE and NARS broadband stations, *Bull. Seismol. Soc. Am.*, *79*(5), 1542–1558.

Weller, O., D. Lange, F. Tilmann, D. Natawidjaja, A. Rietbrock, R. Collings, and L. Gregory (2012), The structure of the Sumatran Fault revealed by local seismicity, *Geophys. Res. Lett.*, *39*, doi:10.1029/2011GL050440.

Wolfe, C. J., and S. C. Solomon (1998), Shear-wave splitting and implications for mantle flow beneath the MELT region of the East Pacific Rise, *Science*, *280*(5367), 1230–1232, doi:10.1126/science.280.5367.1230.

Wüstefeld, A., and G. Bokelmann (2007), Null detection in shear-wave splitting measurements, *Bull. Seismol. Soc. Am.*, *97*(4), 1204–1211, doi:10.1785/0120060190.

Wüstefeld, A., G. Bokelmann, C. Zaroli, and G. Barruol (2008), SplitLab: A shear-wave splitting environment in Matlab, *Comput. Geosci.*, *34*(5), 515–528, doi:10.1016/j.cageo.2007.08.002.

Yardley, G. S., and S. Crampin (1991), Extensive-dilatance anisotropy—Relative information in VSPS and reflection surveys, *Geophys. Prospect.*, *39*(3), 337–355.

Zatsepin, S. V., and S. Crampin (1997), Modeling the compliance of crustal rock .I. Response of shear-wave splitting to differential stress, *Geophys. J. Int.*, *129*(3), 477–494, doi:10.1111/j.1365-246X.1997.tb04488.x.

Zhang, S. Q., and S. Karato (1995), Lattice preferred orientation of olivine aggregates deformed in simple shear, *Nature*, *375*(6534), 774–777, doi:10.1038/375774a0.

Zhang, Z., and S. Y. Schwartz (1994), Seismic anisotropy in the shallow crust of the Loma-Prieta segment of the San-Andreas fault system, *J. Geophys. Res.*, *99*(B5), 9651–9661, doi:10.1029/94JB00241.